

High-ion absorption in seven GRB host galaxies at $z = 2\text{--}4^*$

Evidence for both circumburst plasma and outflowing interstellar gas

A. J. Fox¹, C. Ledoux¹, P. M. Vreeswijk², A. Smette¹, and A. O. Jaunsen³

¹ European Southern Observatory, Alonso de Córdova 3107, Casilla 19001, Vitacura, Santiago, Chile
e-mail: afox@eso.org

² Dark Cosmology Centre, Niels Bohr Institute, University of Copenhagen, Juliane Maries Vej 30, 2100 Copenhagen, Denmark

³ Institute of Theoretical Astrophysics, University of Oslo, PO Box 1029, Blindern, 0315 Oslo, Norway

Accepted 29 May 2008 / Accepted 16 September 2008

ABSTRACT

Aims. We use VLT/UVES high-resolution optical spectroscopy of seven GRB afterglows (at z_{GRB} between 2.20 and 3.97) to investigate circumburst and interstellar plasma in the host galaxies of the bursts.

Methods. GRBs 050730, 050820, 050922C, 060607, 071031, and 080310 were each detected by the *Swift* satellite. With the minimum possible time delay (as short as eight minutes), follow-up optical spectroscopy at 6.0 km s^{-1} resolution began with UVES. We present Voigt-profile component fits and analysis of the high-ion absorption detected in these spectra and in the pre-*Swift* UVES spectrum of GRB 021004, at velocities between $z_{\text{GRB}} - 5000 \text{ km s}^{-1}$ and z_{GRB} .

Results. We identify several distinct categories of high-ion absorption at velocities close to z_{GRB} : (i) strong high-ion absorption at z_{GRB} itself is always seen in O VI, C IV, and Si IV, usually (in six of seven cases) in N V, and occasionally in S IV and S VI. Three of the cases show $\log N(\text{N V}) > 14$ in a single-component, suggesting a circumburst origin, but we cannot rule out an interstellar origin. Indeed, using the non-detection of S IV* at z_{GRB} toward GRB 050730 together with a UV photo-excitation model, we place a lower limit of 400 pc on the distance of the S IV-bearing gas from the GRB; (ii) complex, multi-component C IV and Si IV profiles extending over $100\text{--}400 \text{ km s}^{-1}$ around z_{GRB} are observed in each spectrum; these velocity fields are similar to those measured in C IV in damped Lyman- α systems at similar redshifts, suggesting a galactic origin; (iii) asymmetric, blueshifted, absorption-line wings covering $65\text{--}140 \text{ km s}^{-1}$ are seen in the C IV, Si IV, and O VI profiles in four of the seven GRB afterglow spectra. The wing kinematics together with the “Galactic” C IV/Si IV ratios measured in two cases suggest that the wings trace outflowing interstellar gas in the GRB host galaxies; (iv) high-velocity (HV; $500\text{--}5000 \text{ km s}^{-1}$ relative to z_{GRB}) components are detected in six of the seven spectra; these components are not necessarily a single homogeneous population, and many of them may arise in unrelated foreground galaxies. However, in the cases of GRBs 071031 and 080310, the ionization properties of the HV components (very high C IV/Si IV ratios and absence of neutral-phase absorption in Si II or C II) are suggestive of a circumburst origin; models of Wolf-Rayet winds from the GRB progenitors can explain both the kinematics and ionization level of these HV components.

Key words. gamma rays: bursts – galaxies: halos – galaxies: high-redshift – galaxies: ISM – stars: Wolf-Rayet

1. Introduction

For many years the only backlights available for studying the distant Universe through absorption-line spectroscopy were AGN. Since the discovery that gamma-ray bursts (GRBs) are extragalactic (van Paradijs et al. 1997; Metzger et al. 1997), GRBs have also been employed as backlights, with the advantages of extremely high luminosity and power-law continua, but the disadvantage of rapid temporal fading, implying that rapid-response observations are necessary for their study. Not only do analyses of GRB afterglow spectra allow intervening systems to be studied, they also enable the properties of the interstellar gas in the host galaxy of the GRB to be investigated, particularly its kinematics, chemical abundances, dust content, molecular gas content, and ionized gas content (Castro et al. 2003; Klose et al. 2004; Fiore et al. 2005; Savaglio et al. 2003; Savaglio & Fall 2004; Penprase et al. 2006; Fynbo et al. 2006;

Prochaska et al. 2006, 2007a). Many GRB spectra show damped Lyman- α (DLA) absorption at z_{GRB} , i.e. they show a neutral gas column density $\log N(\text{H I}) > 20.3$ (Jensen et al. 2001; Hjorth et al. 2003; Jakobsson et al. 2004, 2006; Vreeswijk et al. 2004; Starling et al. 2005; Berger et al. 2006; Watson et al. 2006; Prochaska et al. 2007b), typically with higher H I column densities than are seen in DLAs toward QSOs (QSO-DLAs, reviewed by Wolfe et al. 2005). The higher $N(\text{H I})$ in GRB-DLAs may be related to their intense star-formation activity (Bloom et al. 2002), or to the GRB sight-lines passing preferentially through the inner regions of the host galaxies (Fynbo et al. 2008; Prochaska et al. 2008a). Photometric studies of GRB host galaxies have shown them to be star-forming, dwarf galaxies (Christensen et al. 2004; Wiersema et al. 2007; Thöne et al. 2007, 2008a), with no evidence that the hosts are peculiar (Savaglio et al. 2008).

In this paper we use rapid-response mode spectra of seven high-redshift long-duration GRB afterglows to investigate high-ion absorption (in O VI, N V, C IV, Si IV, S IV, and S VI) in the ISM of the host galaxy, as well as in the circumburst medium immediately surrounding the GRB. Observations of ionized interstellar gas in galactic environments provide important

* Based on observations taken under Programme IDs 070.A-0599, 070.D-0523, 075.A-0385, 075.A-0603, 077.D-0661, and 080.D-0526 with the Ultraviolet and Visual Echelle Spectrograph (UVES) on the Very Large Telescope (VLT) Unit 2 (Kueyen) at Paranal, Chile, operated by ESO.

Table 1. GRB sample and log of UVES observations.

GRB (yymmdd)	UT(Trig) ^a	UT(UVES) ^b (hh:mm)	δt^c (hh:mm)	t_{total}^d (s)	ESO ID	z_{GRB}	$\log N_{\text{HI}}^e$	[Z/H] ^e	GCN ^f Refs.	Science ^g Refs.
021004	12:06:13	01:37	13:31	7200	070.A-0599 ^h	2.3290	19.00	0.0	1, 2	3, 4, 5, 6, 7, 8
050730	19:58:23	00:07	04:09	6000	075.A-0603	3.9686	22.15	-2.3	9, 10	8, 11, 12, 13, 14, 15, 16
050820	06:34:53	07:08	00:34	6043	075.A-0385	2.6147	21.00	-0.6	17, 18	8, 13, 15, 16
050922C	19:55:50	23:42	03:47	6000	075.A-0603	2.1990	21.55	-2.0	19, 20	8, 16, 21
060607	05:12:13	05:20	00:08	11980	077.D-0661	3.0749	16.80	0.0	22, 23	8
071031	01:06:36	01:15 ⁱ	00:09	9480	080.D-0526	2.6922	22.15	-1.7	24, 25	...
080310	08:37:58	08:51	00:13	4680	080.D-0526	2.4274	18.80	-1.4	26, 27	...

^a UT of trigger by the BAT instrument on-board *Swift*. Exception: GRB 021004, detected by *WXM* on-board *HETE-2*.

^b UT of start of first UVES exposure (after target acquisition).

^c Time delay between satellite trigger and start of UVES exposure.

^d Total UVES exposure time over all setups.

^e HI column density and metallicity of GRB-DLA taken from reference 8, except 071031 and 080310 values, which are from this paper.

^f We list here the GCN first reporting the burst, and the GCN first reporting the UVES spectrum.

^g We list references relevant to the study of the host galaxy ISM.

^h Also 070.D-0523.

ⁱ Due to a difficult target acquisition, the first fully aligned exposure of GRB 071031 began at 01:25.

References: 1 – Shirasaki et al. (2002); 2 – Savaglio et al. (2002); 3 – Møller et al. (2003); 4 – Mirabal et al. (2003); 5 – Schaefer et al. (2003); 6 – Fiore et al. (2005); 7 – Lazzati et al. (2006); 8 – Prochaska et al. (2008b); 9 – Holland et al. (2005); 10 – D’Elia et al. (2005a); 11 – Starling et al. (2005); 12 – Chen et al. (2005); 13 – Chen et al. (2007); 14 – D’Elia et al. (2007); 15 – Prochaska et al. (2007a); 16 – Prochaska et al. (2007b); 17 – Page et al. (2005); 18 – Ledoux et al. (2005); 19 – Norris et al. (2005); 20 – D’Elia et al. (2005b); 21 – Jakobsson et al. (2006); 22 – Ziaeepeour et al. (2006); 23 – Ledoux et al. (2006); 24 – Stroth et al. (2007); 25 – Ledoux et al. (2007); 26 – Cummings et al. (2008); 27 – Vreeswijk et al. (2008).

constraints on several physical processes, including star formation and subsequent feedback, galactic winds, interactions with satellite galaxies, and accretion. In the pre-*Swift* era, studying high ions in galaxy environments at high redshifts was complicated by the difficulty of associating individual absorbers with individual galaxies. There are several *indirect* ways to explore high-ion absorption in high-redshift galaxies. Firstly, outflowing C IV and Si IV is seen in the composite spectrum of high-redshift Lyman-break galaxies (LBGs, Shapley et al. 2003). Secondly, there is a statistical correlation between the redshifts of C IV absorbers seen in QSO spectra and the redshifts of galaxies near the QSO lines-of-sight (Adelberger et al. 2005). And thirdly, high-ion absorption is detected in all DLAs (Wolfe & Prochaska 2000; Fox et al. 2007a,b; Lehner et al. 2008), which trace galactic structures. However, because of the faintness of high-redshift galaxies, only in a single published case (the lensed LBG cB58; Pettini et al. 2000, 2002) are interstellar high-ion absorption lines seen at moderate-to-high resolution in the spectra of *individual* galaxies at $z > 2$.

Now, with the ability to be on-target within a few minutes of a *Swift* GRB trigger, a new means to directly probe the interstellar (as well as circumburst) medium in individual high-redshift galaxies is available (see Fiore et al. 2005; D’Elia et al. 2007; Chen et al. 2007). High-resolution optical spectroscopy of GRB afterglows now routinely produces spectra with high-enough signal-to-noise to uncover the velocity sub-structure in the absorbing gas. Evidence has even been found for time-variation in the strength of absorption in fine-structure lines at z_{GRB} (Dessauges-Zavadsky et al. 2006; Vreeswijk et al. 2007). In this paper, we present a survey of high-ion absorption in the highest-quality GRB optical afterglow spectra taken to date. We pay particular attention to the high-ion kinematics, since velocity measurements can constrain the presence of gaseous outflows, either from the GRB progenitor or from the host galaxy. We structure this paper as follows. In Sect. 2 we discuss the GRB observations, data processing, and our line profile fitting procedures. In Sect. 3 we describe the observational properties of the high-ion absorption at velocities near z_{GRB} in each afterglow

spectrum. We discuss four distinct observational categories of high-ion absorption in the GRB afterglow spectra in Sect. 4, and we present a summary in Sect. 5.

2. GRB observations

We formed our sample of seven GRB afterglow spectra by selecting all GRBs at $z > 2$ with follow-up high-resolution UVES¹ optical spectroscopy available as of March 2008. Lower redshift GRBs were not considered since no information on the high ions (particularly O VI) is available in these cases. With the exception of GRB 021004, which was detected by the *High-Energy Transient Explorer (HETE-2)* satellite (Ricker et al. 2003), each of the GRBs in our sample was detected by the Burst Alert Telescope (BAT) on-board NASA’s *Swift* satellite (Gehrels et al. 2004). The seven GRBs are 021004, 050730, 050820, 050922C, 060607, 071031, and 080310, named according to the UT date of their detection (yymmdd). Following each trigger, *Swift* began follow-up observations with the XRT and UVOT instruments, to determine an error circle of $\approx 2.5''$ around the source.

After the *Swift* localization was distributed through the GCN (GRB Coordinates Network), rapid-response mode (RRM) UVES observations began on each GRB afterglow with the minimum possible time delay, provided the target was observable from Paranal. Three of the seven GRB afterglows in our sample were observed in this mode. RRM observations involve the immediate interruption of any current UVES exposure in order to slew to and acquire the new target. No human intervention is required, except for alignment of the target on the spectrograph slit. On two occasions, a sub-ten minute response was achieved. These observations demonstrate the power of the RRM concept, and the success of its implementation on ESO telescopes. The four afterglow spectra that were not taken in the RRM mode are GRBs 021004 and 050820, which occurred before the RRM was implemented, and GRBs 050730 and 050922C, which were unobservable from Paranal at the time of the trigger. In each

¹ UVES is described in Dekker et al. (2000).

of these four cases, the UVES observations began at the earliest possible time as conventional Target-of-Opportunity observations. A log of these observations, together with a summary of the basic properties of the GRBs, is given in Table 1.

The spectra were taken with 2×2 binning and a $1.0''$ slit, providing $R \approx 50\,000$ ($FWHM = 6.0 \text{ km s}^{-1}$) spectra in $\approx 2 \text{ km s}^{-1} \text{ pixels}^2$. The UVES data were reduced with a customized version of the MIDAS reduction pipeline (Ballester et al. 2000), with the wavelength scale subsequently corrected into the vacuum heliocentric frame. For the latest GRB in our sample (GRB 080310), we also reduced the data independently with version 3.4.5 of the CPL (Common Pipeline Library) pipeline³. A detailed comparison of line profiles found the results from the two pipeline versions to be essentially identical. Individual exposures were combined with a least-squares weighting to produce a combined spectrum. In the case of GRB 071031, we also maintain and analyze the individual exposures to look for time-series variation (see Sect. 3.6.1). Continua were fit locally to each absorption line of interest. Before displaying and fitting the O VI, C III, NV, and S VI profiles, which fall in low S/N regions of the spectrum, we perform a further rebinning, generally by five pixels, but occasionally by other factors, as described in the captions to Figs. 1 to 4. These differing rebinning factors are driven by the desire to maximize the signal-to-noise ratio and to investigate the significance of the high-ion detections, even if some resolution is compromised.

We searched in each spectrum for high-ion absorption over the velocity range $z_{\text{GRB}} - 5000 \text{ km s}^{-1}$ to $z_{\text{GRB}} + 2000 \text{ km s}^{-1}$, where z_{GRB} is defined by the position of strongest absorption in the low-ionization lines. This wide range was chosen because of the possibility of detecting high-velocity outflow features driven by the burst progenitor. We make a distinction between low-velocity (LV) absorption components seen within several hundred km s^{-1} of z_{GRB} , which are seen in all cases, and high-velocity (HV) components at $500\text{--}5000 \text{ km s}^{-1}$ from z_{GRB} , which are seen in 6/7 sight lines, and which are clearly separated from the LV absorption. When absorption was found, we used the VPFIT software package⁴ to fit the high-ion components in each GRB spectrum with a series of Voigt profiles. Each high ion was fit independently, even species with similar ionization potentials. The VPFIT software accounts for instrumental resolution, and returns the redshift, line width, and column density (z , b , and $\log N$) for each component together with the associated errors. We convert the component redshift to velocity, using z_{GRB} as the zero point. By summing over the component column densities, and adding the component errors in quadrature, we form the total column density and its error in each absorber. In cases where the high-ion absorption is saturated, the errors on the total column density are large. The fit solutions are non-unique, since the number of components to be fit has to be specified manually. This number is often larger than ten, due to the complexity of the absorption-line profiles. Nonetheless, our fitting technique has been tested by comparing the total model column densities with the values from direct apparent optical depth integrations (Fox et al. 2007a). The successful outcome of these tests supports the reliability of the fit results. The details of the fits are given in Tables 2 to 8, for GRBs 021004, 050730,

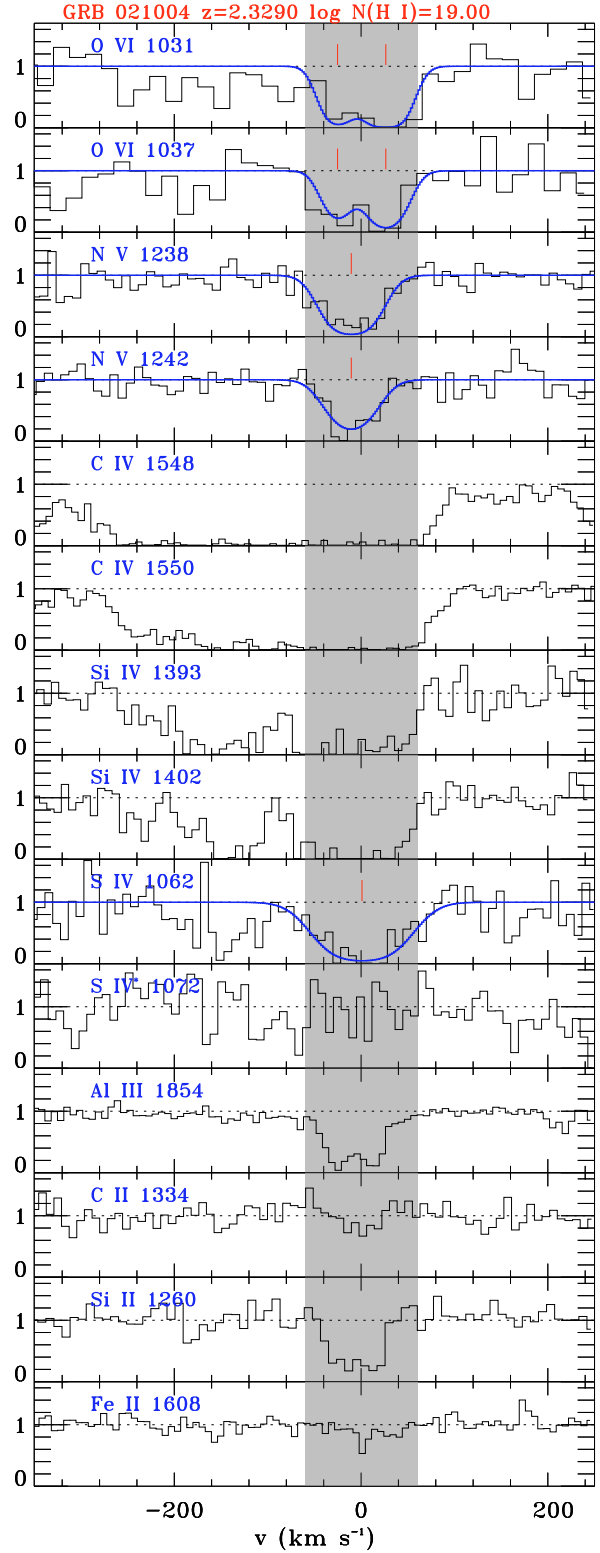


Fig. 1. Normalized high-ion and low-ion absorption-line profiles on a velocity scale relative to z_{GRB} for GRB 021004. Voigt profile fits are shown in blue (solid line), with the center of each component in the fit marked with a red dash. Dark shading denotes the strong absorption components at z_{GRB} . All data have been rebinned by four pixels (eight in the case of O VI). We do not fit the C IV or Si IV doublets because of saturation. Absorption components at higher velocity relative to z_{GRB} are shown in Fig. 5.

² Though the nominal spectral resolution of UVES in this mode is 43 000, we find that a higher resolution of $\approx 50\,000$ is achieved in practice, due to variations in the seeing conditions.

³ See manual at <ftp://ftp.eso.org/pub/dfs/pipelines/uves/uves-pipeline-manual-10.0.pdf>

⁴ Available at <http://www.ast.cam.ac.uk/~rfc/vpfit.html>

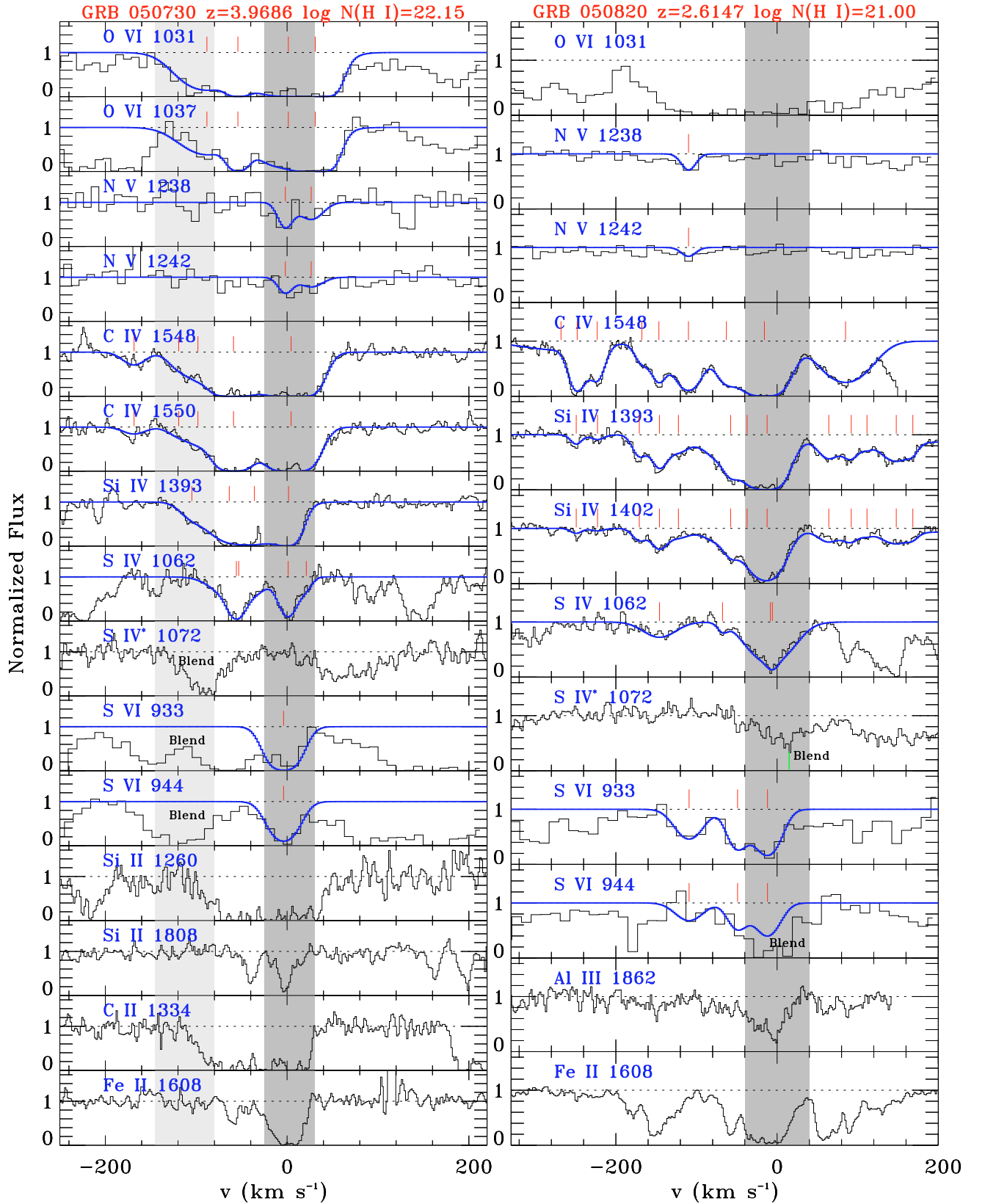


Fig. 2. Normalized high-ion and low-ion absorption-line profiles on a velocity scale relative to z_{GRB} for GRBs 050730 and 050820. Voigt profile fits are shown in blue (solid line), with the center of each component in the fit marked with a red dash. Dark shading denotes the regions of strong absorption at z_{GRB} itself, and light shading denotes the negative-velocity wings (GRB 050730 only). The O VI, N V, and S VI data have been rebinned by five pixels. Absorption components at higher velocity relative to z_{GRB} are shown in Fig. 5.

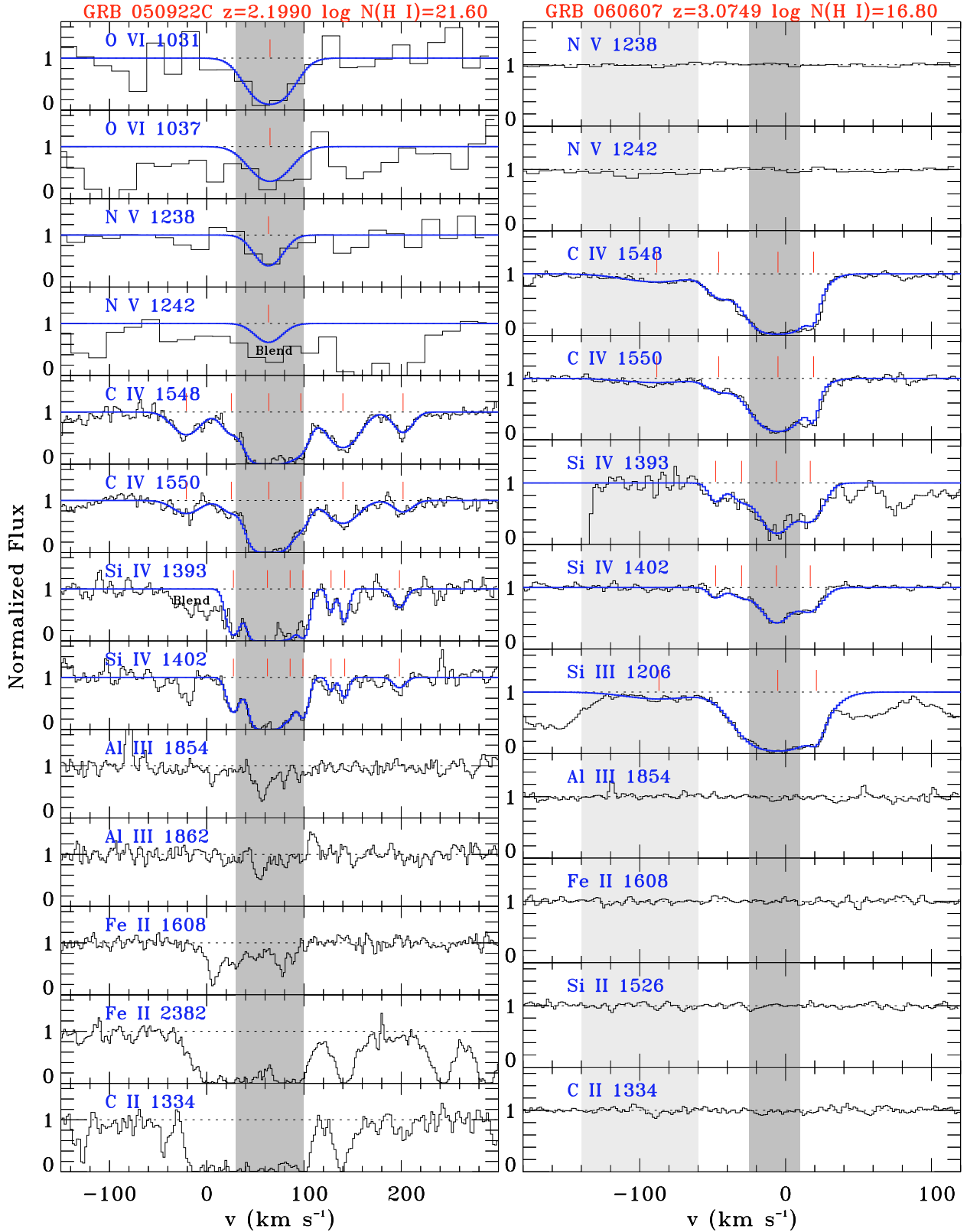


Fig. 3. Normalized high-ion and low-ion absorption-line profiles on a velocity scale relative to z_{GRB} for GRBs 050922C and 060607. Voigt profile fits are shown in blue (solid line), with the center of each component in the fit marked with a red dash. Dark shading denotes the regions of strong absorption, and light shading denotes the negative-velocity wing (GRB 060607 only). The S IV and S VI profiles are blended in each of these sight lines. The O VI and N V data have been rebinned by eight pixels for GRB 050922C, and the N V data by five pixels for GRB 060607. Absorption components at higher velocity relative to z_{GRB} are shown in Fig. 5.

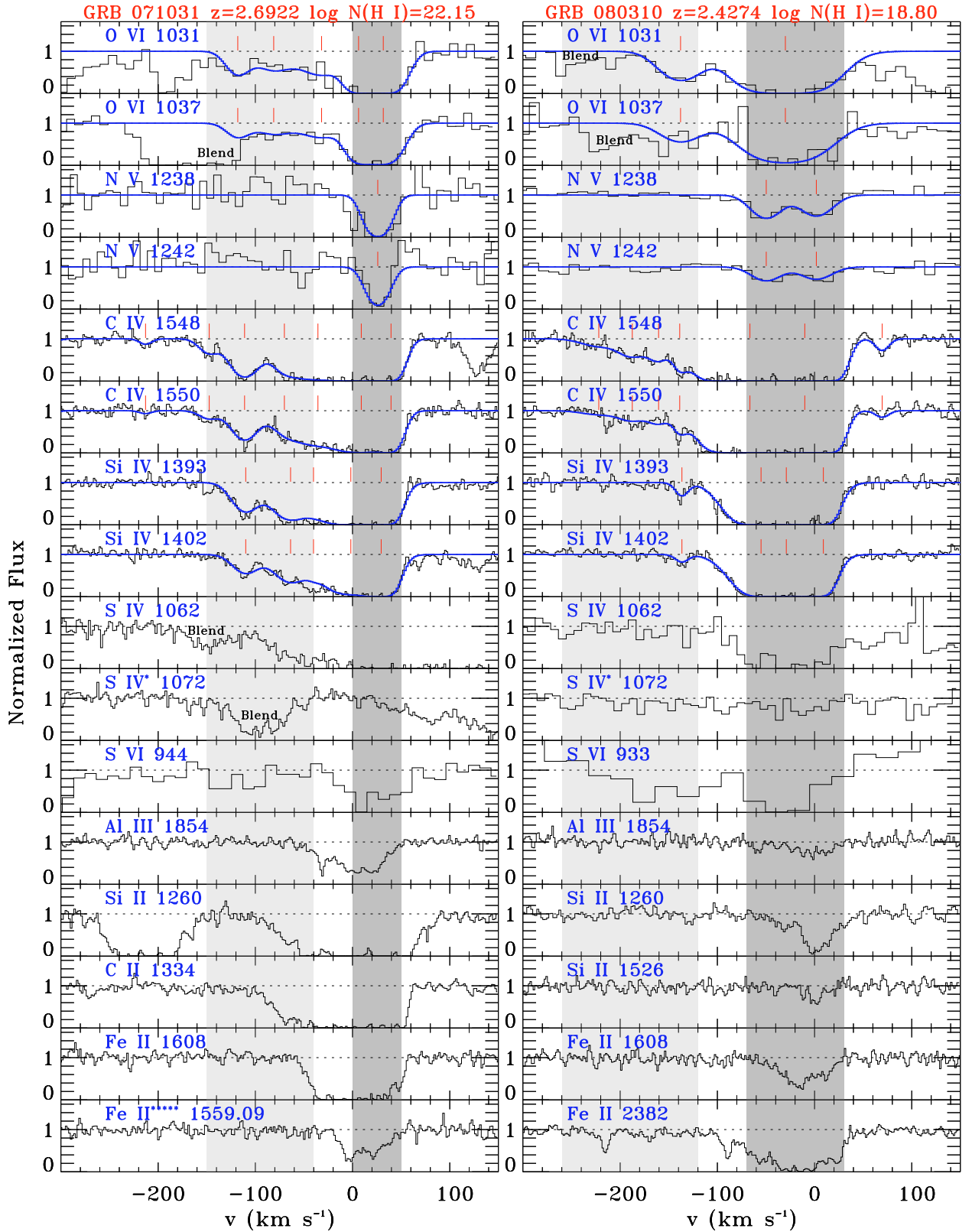


Fig. 4. Normalized high-ion and low-ion absorption-line profiles on a velocity scale relative to z_{GRB} for GRBs 071031 and 080310. Voigt profile fits are shown in blue (solid line), with the center of each component in the fit marked with a red dash. Dark shading denotes the regions of strong absorption, and light shading denotes the negative-velocity wings. The O VI and N V data have been rebinned by four pixels for GRB 071031 and by five pixels for GRB 080310. For S VI, the rebin factors are five and ten, respectively. Absorption components at higher velocity relative to z_{GRB} are shown in Fig. 5.

Table 2. GRB 021004 $z = 2.3290$: Voigt profile fits.

Ion	v_0 (km s ⁻¹)	b (km s ⁻¹)	$\log N$ (N in cm ⁻²)	$\log N(\text{total})$ (N in cm ⁻²)
O VI	-25 ± 8	18 ± 10	14.46 ± 0.22	14.95 ± 0.20
...	26 ± 7	22 ± 8	14.78 ± 0.22	...
N V	-2903 ± 2	19 ± 2	14.03 ± 0.05	14.03 ± 0.05
N V	-10 ± 2	28 ± 3	14.53 ± 0.06	14.53 ± 0.06
C IV	-2966 ± 4	12 ± 6	12.97 ± 0.19	14.73 ± 0.08
...	-2903 ± 2	30 ± 2	14.59 ± 0.04	...
...	-2720 ± 2	8 ± 2	13.36 ± 0.09	...
...	-2670 ± 2	31 ± 3	14.03 ± 0.04	...
...	-2599 ± 8	24 ± 11	13.10 ± 0.18	...
Si IV	-2903 ± 3	*	*	$\approx 14.82^*$
...	-2882 ± 45	58 ± 40	13.53 ± 0.42	...
...	-2659 ± 4	20 ± 5	13.20 ± 0.10	...
S IV	0 ± 4	45 ± 5	15.25 ± 0.20	15.25 ± 0.20

Note: the symbol * denotes a saturated component; no reliable column density or line width can be extracted for the component, and the total column density in that ion is uncertain. Note: total column densities (summed over components) are reported separately for the HV and LV absorption. Note: No C IV or Si IV fit was attempted to the absorption within 1000 km s⁻¹ of z_{GRB} , due to complete saturation.

050820, 050922C, 060607, 071031, and 080310, respectively. Atomic data (rest wavelengths and f -values) were taken from Morton (2003).

3. Description of the high-ion absorption

High-ion absorption within several hundred km s⁻¹ of z_{GRB} is found in all seven GRB spectra in our sample. The detected lines are C IV and Si IV (seen in 7/7 cases), N V (6/7), O VI (6/7), S IV (5/7), and S VI (2/7). The high-ion absorption-line profiles in the velocity range within 200 km s⁻¹ of z_{GRB} are shown for each of our seven GRB afterglow spectra in Figs. 1 to 4. In addition to the high ions, we include on each figure absorption lines that trace the neutral gas, typically Si II $\lambda 1260.422$, C II $\lambda 1334.532$, or Fe II $\lambda 1608.451$.

In cases where we do not report a detection for O VI, S IV, and S VI (e.g. O VI toward GRB 060607), it is because the profiles are blended, not because there are actual non-detections in these ions. The only clear non-detection at z_{GRB} in any of the high ions mentioned above is in N V toward GRB 060607. In two cases our data cover the wavelength of Ne VIII $\lambda 770.409$, 780.324 at z_{GRB} , but the doublet lies below the Lyman limit where no flux is transmitted. P V $\lambda 1117.977$, 1128.008 is not detected in any of the seven spectra. C III $\lambda 977.020$ is detected in one case (GRB 071031), but in the other sight lines the S/N is too low at the observed wavelength (far into the blue) for the C III data to be useful. Absorption in S IV* $\lambda 1072.973$ is not observed in any of the seven spectra. Finally, with the exception of GRB 060607 with its unusually low $N(\text{H I})$, Si III $\lambda 1206.500$ lies in the strong damping wings of Lyman- α , so no useful information on this ion at z_{GRB} is available.

The detection rate of N V in our sample is identical to that reported by Prochaska et al. (2008b), who find N V at z_{GRB} in 6/7 GRB afterglow spectra, but since five systems are common to both samples, this is not surprising. N V has also been detected at z_{GRB} in the afterglow spectrum of GRB 060206 (Thöne et al. 2008b). Other than the O VI absorption in the GRB 050730 spectrum, which has been published by D’Elia et al. (2007), no reports of O VI at z_{GRB} in GRB afterglow spectra exist, and no

Table 3. GRB 050730 $z = 3.9686$: Voigt profile fits.

Ion	v_0 (km s ⁻¹)	b (km s ⁻¹)	$\log N$ (N in cm ⁻²)	$\log N(\text{total})$ (N in cm ⁻²)
O VI	-88 ± 5	34 ± 5	14.52 ± 0.08	$\approx 15.94^*$
...	-54 ± 2	*	*	...
...	1 ± 8	36 ± 6	14.97 ± 0.15	...
...	31 ± 6	*	*	...
N V	-1 ± 2	7 ± 3	13.54 ± 0.15	13.80 ± 0.14
...	26 ± 5	14 ± 8	13.46 ± 0.18	...
C IV	-1577 ± 2	4 ± 2	13.38 ± 0.22	14.52 ± 0.18
...	-1567 ± 2	5 ± 4	13.43 ± 0.23	...
...	-1553 ± 2	5 ± 2	13.66 ± 0.17	...
...	-1536 ± 2	12 ± 2	13.97 ± 0.10	...
...	-1516 ± 2	34 ± 34	13.81 ± 0.37	...
...	-1480 ± 2	11 ± 3	13.86 ± 0.17	...
C IV	-168 ± 2	14 ± 3	13.12 ± 0.06	$\approx 15.24^*$
...	-119 ± 18	*	*	...
...	-98 ± 7	*	*	...
...	-58 ± 2	17 ± 3	14.81 ± 0.10	...
...	4 ± 2	21 ± 2	15.01 ± 0.06	...
Si IV	-1575 ± 2	4 ± 2	12.57 ± 0.06	13.94 ± 0.10
...	-1553 ± 2	4 ± 2	13.03 ± 0.05	...
...	-1542 ± 3	26 ± 3	13.38 ± 0.08	...
...	-1529 ± 2	7 ± 4	12.45 ± 0.38	...
...	-1499 ± 2	9 ± 4	12.61 ± 0.21	...
...	-1472 ± 2	12 ± 2	13.50 ± 0.03	...
...	-1442 ± 2	13 ± 2	13.02 ± 0.04	...
Si IV	-104 ± 6	*	*	$\approx 14.35^*$
...	-63 ± 50	*	*	...
...	-35 ± 50	*	*	...
...	1 ± 2	10 ± 2	13.94 ± 0.12	...
S IV	-53 ± 2	28 ± 4	14.51 ± 0.06	$\approx 15.31^*$
...	-55 ± 2	*	*	...
...	1 ± 2	8 ± 2	14.65 ± 0.06	...
...	21 ± 2	4 ± 3	13.57 ± 0.15	...
S VI	-3 ± 2	17 ± 2	14.16 ± 0.06	14.16 ± 0.06

Note: the symbol * denotes a saturated component; no reliable column density or line width can be extracted for the component, and the total column density in that ion is uncertain. Note: total column densities (summed over components) are reported separately for the HV and LV absorption.

previous reports of S IV or S VI exist either. Indeed, very few reports of interstellar S VI absorption exist anywhere in the high- z (Churchill & Charlton 1999; Levshakov et al. 2003) or low- z (Savage et al. 2005b) Universe. Interstellar S IV absorption-line detections have (to our knowledge) only been reported in quasar-intrinsic systems (Arav et al. 1999; Ganguly et al. 2006). Finally, our non-detections of absorption in S IV* $\lambda 1072.973$ contrast with detections of this line in the winds of OB-type stars (Massa et al. 2003; Lehner et al. 2003).

The absorption features observed at and near z_{GRB} can be classified into various types. First, strong absorption is seen exactly at z_{GRB} in the form of saturated O VI, C IV, and Si IV lines, usually with accompanying N V, and (where the data are unblended) also in S IV and S VI. Second, complex multi-component C IV and Si IV profiles with total velocity widths of 100–400 km s⁻¹ are seen in all seven GRB afterglow spectra. Third, 4/7 GRB afterglow spectra show asymmetric negative-velocity absorption-line wings extending over velocity regions of 65–140 km s⁻¹. These wings are seen clearest in C IV and Si IV, but are also present in O VI. Fourth, 6/7 cases show HV components in C IV, and occasionally also in neutral-phase lines such as Si II and C II. Whereas the first three of these categories are visible in Figs. 1 to 4, we present a separate plot (Fig. 5)

Table 4. GRB 050820 $z = 2.6147$: Voigt profile fits.

Ion	v_0 (km s ⁻¹)	b (km s ⁻¹)	$\log N$ (N in cm ⁻²)	$\log N(\text{total})$ (N in cm ⁻²)
N V	-109 ± 2	9 ± 3	13.17 ± 0.08	13.17 ± 0.08
C IV	-3655 ± 2	10 ± 2	13.02 ± 0.04	13.13 ± 0.06
...	-3631 ± 2	10 ± 3	12.50 ± 0.11	...
C IV	-268 ± 6	65 ± 8	13.42 ± 0.05	14.91 ± 0.11
...	-247 ± 2	9 ± 2	13.87 ± 0.03	...
...	-223 ± 2	9 ± 2	13.53 ± 0.03	...
...	-167 ± 2	9 ± 2	13.13 ± 0.07	...
...	-146 ± 2	9 ± 2	13.58 ± 0.04	...
...	-109 ± 2	18 ± 2	14.02 ± 0.02	...
...	-62 ± 2	15 ± 2	13.74 ± 0.06	...
...	-15 ± 2	25 ± 2	14.55 ± 0.04	...
...	84 ± 2	35 ± 2	14.06 ± 0.02	...
Si IV	-249 ± 2	5 ± 2	12.23 ± 0.05	14.35 ± 0.18
...	-222 ± 2	8 ± 3	11.98 ± 0.10	...
...	-170 ± 2	8 ± 2	12.72 ± 0.04	...
...	-145 ± 2	10 ± 2	13.05 ± 0.06	...
...	-122 ± 3	13 ± 4	12.67 ± 0.14	...
...	-57 ± 2	7 ± 2	12.74 ± 0.14	...
...	-37 ± 3	46 ± 3	13.72 ± 0.08	...
...	-12 ± 2	20 ± 2	14.00 ± 0.04	...
...	64 ± 2	16 ± 2	12.96 ± 0.06	...
...	91 ± 2	11 ± 3	12.82 ± 0.09	...
...	111 ± 2	4 ± 3	12.14 ± 0.20	...
...	147 ± 2	26 ± 3	13.23 ± 0.05	...
...	168 ± 2	4 ± 3	12.05 ± 0.19	...
...	220 ± 2	4 ± 2	12.39 ± 0.13	...
...	202 ± 6	17 ± 12	12.32 ± 0.29	...
S IV	-145 ± 2	25 ± 3	14.04 ± 0.04	14.91 ± 0.07
...	-67 ± 2	4 ± 3	13.30 ± 0.10	...
...	-5 ± 2	4 ± 2	14.04 ± 0.12	...
...	-8 ± 2	32 ± 2	14.76 ± 0.03	...
S VI	-109 ± 3	20 ± 4	13.45 ± 0.07	14.09 ± 0.08
...	-49 ± 3	14 ± 3	13.54 ± 0.11	...
...	-11 ± 3	17 ± 3	13.77 ± 0.07	...

Note: total column densities (summed over components) are reported separately for the HV and LV absorption. Note: S VI is only detected in $\lambda 933$ ($\lambda 944$ is blended), so the detection is uncertain. Nonetheless the velocity structure corresponds closely to C IV.

showing the HV high-ion absorbers detected in our sample. We return to a discussion of these categories of absorption in Sect. 4, after describing the details of the high-ion absorption in each spectrum. Unless otherwise stated, solar abundances were taken from [Lodders \(2003\)](#).

3.1. GRB 021004 $z_{\text{GRB}} = 2.3290$

Extremely strong C IV absorption is seen at z_{GRB} , with a fully saturated trough spreading over 300 km s^{-1} . Si IV is also present and less saturated than C IV, but we cannot discern the true component structure in Si IV because of low S/N. A component centered at 0 km s^{-1} is seen in O VI, N V, and S IV, with absorption also detected in Al III, Si II, C II, and Fe II. S IV* $\lambda 1072.973$ is not detected at z_{GRB} ; we measure $\log N(\text{S IV}^*) < 14.19$ (3σ) over the velocity range -60 to 60 km s^{-1} , and $\log N(\text{S IV}) = 15.30 \pm 0.29$, so that $N(\text{S IV}^*)/N(\text{S IV}) < 0.08$. Two HV absorbers are observed: one centered at -2900 km s^{-1} relative to z_{GRB} , the other centered at $\approx -600 \text{ km s}^{-1}$. The first is seen in Si IV, C IV, N V, Si II, and C II. The second is seen in C IV, Si IV, and Si II. These two HV absorption-line complexes are shown in separate columns in Fig. 5. The O VI data are too blended in the HV components to be of use. A full study of the UVES spectrum of GRB 021004

Table 5. GRB 050922C $z = 2.1990$: Voigt profile fits.

Ion	v_0 (km s ⁻¹)	b (km s ⁻¹)	$\log N$ (N in cm ⁻²)	$\log N(\text{total})$ (N in cm ⁻²)
O VI	65 ± 2	24 ± 2	14.44 ± 0.05	14.44 ± 0.05
N V	63 ± 2	16 ± 3	13.76 ± 0.07	13.76 ± 0.07
C IV	-20 ± 2	16 ± 2	13.39 ± 0.03	15.69 ± 0.35
...	25 ± 2	10 ± 2	13.21 ± 0.08	...
...	63 ± 2	11 ± 2	15.67 ± 0.30	...
...	96 ± 2	8 ± 2	13.63 ± 0.07	...
...	140 ± 2	18 ± 2	13.73 ± 0.03	...
...	201 ± 2	10 ± 2	13.18 ± 0.04	...
Si IV	27 ± 2	7 ± 2	13.22 ± 0.04	14.49 ± 0.16
...	62 ± 2	12 ± 2	14.40 ± 0.11	...
...	85 ± 2	5 ± 3	13.13 ± 0.24	...
...	98 ± 2	6 ± 2	13.28 ± 0.05	...
...	127 ± 2	4 ± 2	12.42 ± 0.07	...
...	141 ± 2	4 ± 2	12.70 ± 0.05	...
...	198 ± 2	7 ± 2	12.53 ± 0.07	...

Table 6. GRB 060607 $z = 3.0749$: Voigt profile fits.

Ion	v_0 (km s ⁻¹)	b (km s ⁻¹)	$\log N$ (N in cm ⁻²)	$\log N(\text{total})$ (N in cm ⁻²)
C IV	-1849 ± 2	9 ± 2	13.70 ± 0.03	13.83 ± 0.05
...	-1824 ± 2	18 ± 2	13.23 ± 0.05	...
C IV	-88 ± 3	31 ± 4	13.00 ± 0.05	15.94 ± 0.32
...	-45 ± 2	10 ± 2	13.03 ± 0.06	...
...	-5 ± 2	19 ± 2	14.26 ± 0.02	...
...	19 ± 2	4 ± 2	15.93 ± 0.28	...
Si IV	-1848 ± 2	11 ± 2	13.12 ± 0.04	13.28 ± 0.06
...	-1817 ± 2	12 ± 3	12.76 ± 0.07	...
Si IV	-47 ± 2	4 ± 2	12.31 ± 0.12	13.54 ± 0.09
...	-30 ± 3	8 ± 5	12.48 ± 0.23	...
...	-6 ± 2	12 ± 2	13.30 ± 0.06	...
...	16 ± 2	10 ± 2	12.98 ± 0.07	...

Note: total column densities (summed over components) are reported separately for the HV and LV absorption.

is presented by [Fiore et al. \(2005\)](#), and possible origins of the HV components (e.g. a series of shells around the progenitor star) are discussed in [Møller et al. \(2002\)](#), [Mirabal et al. \(2003\)](#), [Schaefer et al. \(2003\)](#), and [Lazzati et al. \(2006\)](#). The velocity difference between the absorber at z_{GRB} and the HV absorber near -500 km s^{-1} is equal to the velocity difference between the two lines of the C IV doublet, i.e. line-locking is observed in C IV (first noticed by [Møller et al. 2002](#))⁵.

3.2. GRB 050730 $z_{\text{GRB}} = 3.9686$

High-ion absorption is seen in O VI, N V, C IV, Si IV, S IV, and S VI centered at z_{GRB} . All of these lines except N V are saturated. The N V profile shows two components separated by $27 \pm 5 \text{ km s}^{-1}$, each with fairly narrow b -values (7 ± 3 and $14 \pm 8 \text{ km s}^{-1}$); we fit the S VI absorption with one component with $b = 17 \pm 2 \text{ km s}^{-1}$. S IV* $\lambda 1072.973$ is not detected at z_{GRB} ; we measure $\log N(\text{S IV}^*) < 13.70$ (3σ) over the velocity range -25 to 20 km s^{-1} , in which we measure $\log N(\text{S IV}) = 14.61 \pm 0.15$, so that $N(\text{S IV}^*)/N(\text{S IV}) < 0.12$. Note that this limit applies only to the strongest component of

⁵ Line-locking is understood as occurring when a cloud is accelerated by radiation pressure in a given doublet line until the wavelength shifts into the shadow of the other doublet line cast by a separate cloud ([Vilkoviskij et al. 1999](#)).

Table 7. GRB 071031 $z = 2.6922$: Voigt profile fits.

Ion	v_0 (km s ⁻¹)	b (km s ⁻¹)	$\log N$ (N in cm ⁻²)	$\log N(\text{total})$ (N in cm ⁻²)
O VI	-560 ± 3	18 ± 3	14.52 ± 0.08	14.77 ± 0.08
...	-505 ± 2	14 ± 2	14.41 ± 0.06	...
O VI	-118 ± 7	13 ± 12	13.79 ± 0.42	$\approx 15.14^*$
...	-81 ± 15	*	*	...
...	-31 ± 12	*	*	...
...	6 ± 14	*	*	...
...	31 ± 15	*	*	...
N V	25 ± 2	11 ± 2	14.41 ± 0.15	14.41 ± 0.15
C IV	-566 ± 2	*	*	$\approx 14.40^*$
...	-559 ± 5	10 ± 3	13.06 ± 0.27	...
...	-515 ± 3	*	*	...
...	-505 ± 4	7 ± 3	13.67 ± 0.24	...
...	-368 ± 2	12 ± 2	13.93 ± 0.03	...
...	-325 ± 2	16 ± 3	13.14 ± 0.05	...
C IV	-212 ± 2	4 ± 3	12.47 ± 0.11	$\approx 15.11^*$
...	-147 ± 2	11 ± 2	13.13 ± 0.06	...
...	-111 ± 2	14 ± 2	13.96 ± 0.08	...
...	-70 ± 6	*	*	...
...	-35 ± 14	33 ± 30	14.43 ± 0.44	...
...	8 ± 7	22 ± 5	14.69 ± 0.22	...
...	39 ± 5	8 ± 3	14.58 ± 0.36	...
Si IV	-367 ± 2	6 ± 2	12.33 ± 0.08	12.33 ± 0.08
Si IV	-109 ± 2	15 ± 2	13.28 ± 0.03	15.93 ± 0.51
...	-63 ± 2	19 ± 3	13.61 ± 0.07	...
...	-40 ± 2	4 ± 16	15.89 ± 0.48	...
...	-1 ± 3	29 ± 3	14.22 ± 0.07	...
...	29 ± 3	11 ± 2	14.65 ± 0.24	...
C III	-560 ± 2	15 ± 3	13.20 ± 0.07	$\approx 14.47^*$
...	-507 ± 2	*	*	...
...	-367 ± 2	*	*	...

Note: the symbol * denotes a saturated component; no reliable column density or line width can be extracted for the component, and the total column density in that ion is uncertain. Note: total column densities (summed over components) are reported separately for the HV and LV absorption. Note: O VI is only detected at -118 km s⁻¹ in $\lambda 1031$ ($\lambda 1037$ is blended), so the detection in this component is uncertain.

absorption. The C IV, Si IV, O VI, and C II profiles show a clear negative-velocity absorption-line wing extending from -70 to -145 km s⁻¹. Finally, a HV absorber at -1550 km s⁻¹ is seen with at least five Si IV and C IV components spread over ≈ 200 km s⁻¹ (see also [Chen et al. 2007](#)). This HV absorption-line complex is shown in Fig. 5. This GRB shows an extremely high H I column of $\log N(\text{H I}) = 22.15$, and is the highest redshift GRB in our sample. A full study of the neutral and excited-state lines at z_{GRB} in the UVES spectrum of GRB 050730 is presented by [D’Elia et al. \(2007\)](#).

3.3. GRB 050820 $z_{\text{GRB}} = 2.6147$

N V shows a single narrow component at -109 km s⁻¹ relative to z_{GRB} with $b = 9 \pm 3$ km s⁻¹. This N V- z_{GRB} offset is the largest among our seven spectra, and has been noticed before ([Prochaska et al. 2008b](#)), but the formal significance of the $\lambda 1238.821$ and $\lambda 1242.804$ detections is only 3.1σ and 2.0σ respectively. The C IV and Si IV profiles exhibit at least ten components spread over 400 km s⁻¹ in velocity width, with a C IV/Si IV ratio that changes dramatically between components. C IV $\lambda 1550.781$ is blended so we only

Table 8. GRB 080310 $z = 2.4274$: Voigt profile fits.

Ion	v_0 (km s ⁻¹)	b (km s ⁻¹)	$\log N$ (N in cm ⁻²)	$\log N(\text{total})$ (N in cm ⁻²)
O VI	-137 ± 4	25 ± 5	14.18 ± 0.08	15.12 ± 0.09
...	-30 ± 3	42 ± 4	15.07 ± 0.08	...
N V	-49 ± 2	18 ± 3	13.75 ± 0.05	14.03 ± 0.05
...	1 ± 2	19 ± 3	13.71 ± 0.05	...
C IV	-1414 ± 2	4 ± 2	12.89 ± 0.10	13.45 ± 0.08
...	-1388 ± 4	33 ± 5	13.31 ± 0.07	...
C IV	-222 ± 16	22 ± 14	13.03 ± 0.41	$\approx 16.66^*$
...	-187 ± 4	17 ± 10	13.36 ± 0.31	...
...	-160 ± 3	11 ± 4	13.33 ± 0.25	...
...	-138 ± 2	5 ± 2	13.44 ± 0.36	...
...	-66 ± 50	*	*	...
...	-10 ± 50	*	*	...
...	69 ± 2	5 ± 2	12.88 ± 0.08	...
Si IV	-136 ± 2	4 ± 2	12.53 ± 0.05	$\approx 15.00^*$
...	-55 ± 50	*	*	...
...	-29 ± 19	*	*	...
...	9 ± 18	*	*	...

Note: the symbol * denotes a saturated component; no reliable column density or line width can be extracted for the component, and the total column density in that ion is uncertain. Note: total column densities (summed over components) are reported separately for the HV and LV absorption.

display C IV $\lambda 1548.204$. A similar velocity structure is observed at lower S/N in Al III $\lambda 1862.789$. S VI $\lambda 933.378$ shows three components aligned with three components seen in C IV, strongly suggesting the genuine presence of S VI. However, S VI $\lambda 944.523$ is affected by low S/N and possible blending, so we treat the S VI detection as marginal. The O VI profiles are highly blended and/or saturated, except for the range -140 and -200 km s⁻¹ in O VI $\lambda 1031.926$, where the profile closely follows the shape of the C IV and Si IV profile. Therefore while we are not able to measure the O VI absorption in this case, we know that it is present. S IV $\lambda 1062.662$ shows a profile that broadly follows the Si IV. The S IV* $\lambda 1072.973$ profile is difficult to interpret. An absorption feature at 15 km s⁻¹ does not correspond to any component in any other high ion, so we identify it as a blend. However, we cannot rule out the presence of genuine S IV* absorption between -50 and 0 km s⁻¹. Finally a two-component HV absorber at -3660 km s⁻¹ relative to z_{GRB} is seen in C IV, but with no detectable Si IV, C II, or Si II (see Fig. 5).

3.4. GRB 050922C $z_{\text{GRB}} = 2.1990$

A single, strong component in O VI, N V, C IV and Si IV is detected at 65 km s⁻¹ relative to z_{GRB} . Al III is also detected in this component in both $\lambda 1854.716$ and $\lambda 1862.789$. Our best-fit to the O VI line has $b = 24 \pm 2$ km s⁻¹; for the N V line, we find $b = 16 \pm 3$ km s⁻¹. C IV and Si IV show a complex series of at least six components spread over ≈ 280 km s⁻¹, but with no evidence for a negative-velocity wing. The S IV and S VI data are blended and not shown in Fig. 3. This GRB shows a high $\log N(\text{H I})$ value of 21.60 , and a low metallicity of -2.0 ([Prochaska et al. 2008b](#)). This is the only GRB afterglow spectrum in our sample in which no HV C IV components are detected.

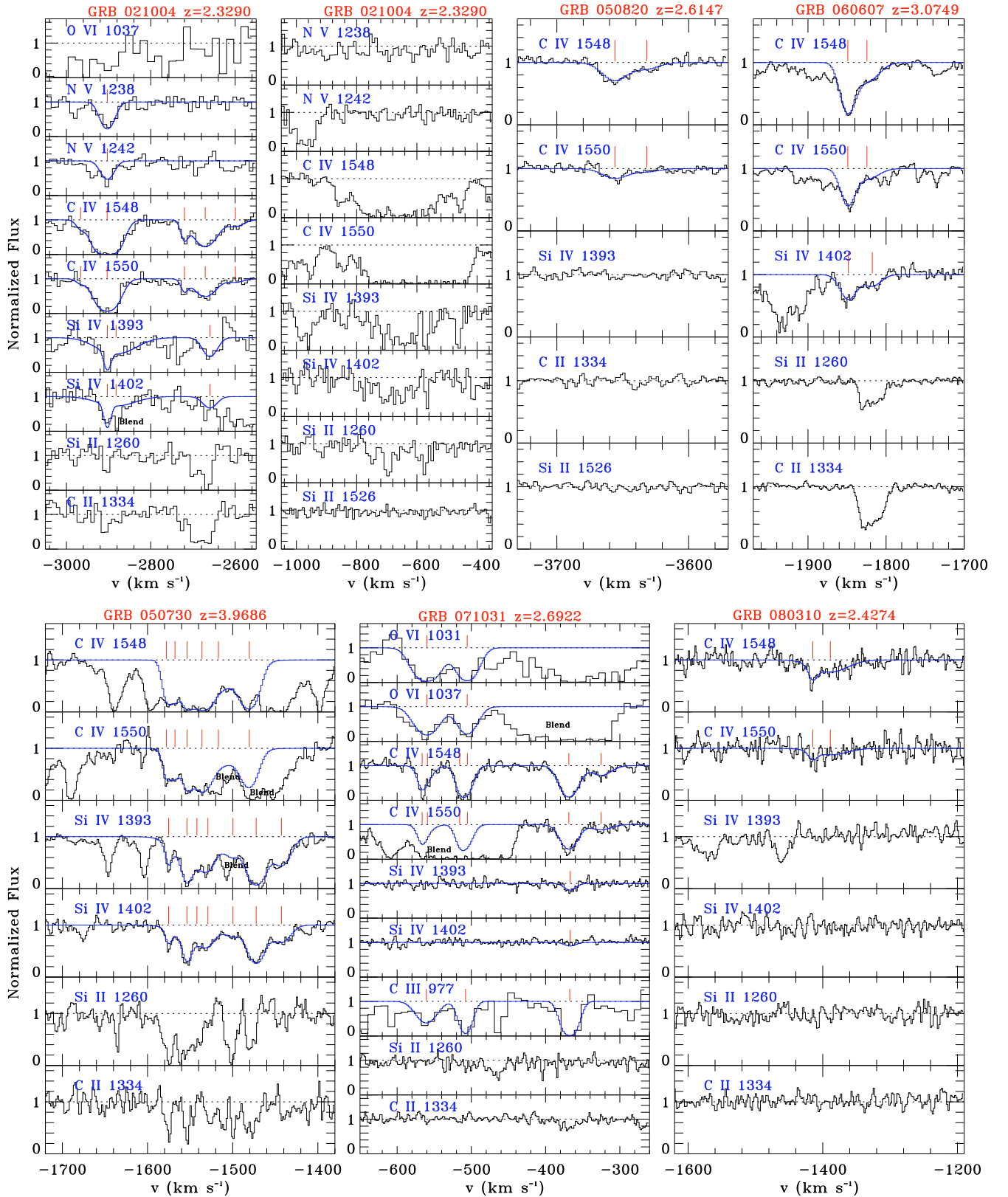


Fig. 5. Seven high-velocity ($500\text{--}5000\text{ km s}^{-1}$ from z_{GRB}) high-ion absorbers are seen in the seven GRB afterglow spectra in our sample; these HV absorbers are shown here (GRB 021004 shows two HV absorbers, GRB 050922C shows none, and the other five GRB spectra show one each). Voigt profile fits are only shown (with blue solid lines) for cases where we judge that reliable column densities can be extracted. The properties of these HV absorbers are diverse, and it is unlikely that they represent a single population. Several of these HV absorbers are seen in both neutral-phase and high-ion-phase absorption; others (e.g. the HV components toward GRB 071031 and GRB 080310) are seen only in high-ion transitions.

3.5. GRB 060607 $z_{\text{GRB}} = 3.0749$

The high ions in the GRB 060607 spectrum behave differently than in the other afterglow spectra. The C IV, Si IV, and Si III profiles show a four-component absorber centered at z_{GRB} and covering only $\approx 100 \text{ km s}^{-1}$ of total width. However, NV is not detected at z_{GRB} ; we derive a 3σ upper limit of $\log N(\text{NV}) < 12.70$ in the velocity range -140 to 50 km s^{-1} , where C IV absorption is seen. The O VI, S IV, and S VI data are blended near z_{GRB} and are of no use. Al III shows a non-detection. The C IV profiles also show a weak (low optical depth) wing extending from -60 to -120 km s^{-1} . This GRB has an extremely low HI column density, $\log N(\text{HI}) = 16.8$ (Prochaska et al. 2008b), 3.5 orders of magnitude lower than the DLA columns seen in five of the other six cases. A HV absorber seen in C IV and Si IV is centered at -1850 km s^{-1} relative to z_{GRB} , with nearby low-ion absorption present in Si II and C II (Fig. 5).

We note that a sub-DLA at $z = 2.9372$ is detected in the GRB 060607 spectrum with $\log N(\text{HI}) = 19.50 \pm 0.05$ (first noticed by Ledoux et al. 2006). This sub-DLA is separated from the nominal GRB redshift of 3.0749 by $\Delta z = 0.1377$, or 10300 km s^{-1} , and shows strong, multi-component absorption in O VI, C IV, and Si IV. We considered the possibility that the host galaxy of GRB 060607 is actually located at this redshift ($z = 2.9372$), which would imply its ISM properties are more similar to those of the host galaxy ISM of the other bursts in our sample. However, this hypothesis is unlikely to be correct since (a) Lyman- α forest lines are detected up to the redshift of 3.0749, suggesting that z_{GRB} really is this high, and (b) this scenario would require the absorber observed at $z = 3.0749$ to be in front of the host galaxy yet moving toward it at over 10000 km s^{-1} , which is not easy to explain dynamically. We conclude that the sub-DLA at 2.9372 traces a foreground galaxy unrelated to the GRB.

3.6. GRB 071031 $z_{\text{GRB}} = 2.6922$

A strong component in O VI, NV, C IV, and Si IV is detected at z_{GRB} . The least-saturated high-ion line, NV, shows a narrow line width of $b(\text{NV}) = 11 \pm 2 \text{ km s}^{-1}$, implying $\log T < 5.08$ for the gas containing the N^{+4} ions, regardless of ionization mechanism. No information is available on the line widths of C IV and Si IV at z_{GRB} because the absorption in these lines is saturated. Whereas S VI $\lambda 933.378$ is blended, S VI $\lambda 944.523$ appears to show absorption at z_{GRB} , with a profile that matches that of O VI. However, because of the low S/N of the data at these wavelengths, we do not attempt to derive a S VI column density. We measure $\log N(\text{Si IV}^*) < 13.87$ (3σ) over the velocity range 0 to 50 km s^{-1} , but complete saturation (and possible blending) prevents a reliable measurement of $\log N(\text{Si IV})$ in this velocity range. Absorption in several fine-structure lines of Fe, Ni, O, Si, and C is detected at z_{GRB} in the GRB 071031 afterglow spectrum: in Fig. 4 we show a line (Fe II^{*****} $\lambda 1559.085$) from the fifth excited level ($^4\text{F}_{9/2}$) of Fe II. We derive an HI column density $\log N(\text{HI}) = 22.15 \pm 0.05$ and a metallicity $[\text{Zn}/\text{H}]$ of -1.72 ± 0.06 , where zinc is chosen since it is typically undetected onto interstellar dust grains.

A notable feature of the C IV, Si IV, S IV, and (at lower S/N) the O VI profiles is the wing extending blueward from 0 km s^{-1} down to -160 km s^{-1} . A component at -115 km s^{-1} is superimposed on the wing. The C IV and Si IV profiles follow one another closely, suggesting these two ions form in the same physical regions of gas. However, the slope $dN_a(v)/dv$ is

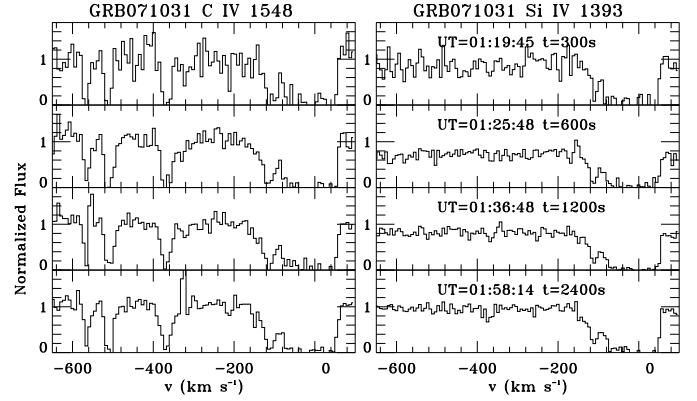


Fig. 6. Time-series observations of C IV and Si IV absorption in the GRB 071031 afterglow spectra. Each row shows a different observing epoch, with the UT of the start of each exposure annotated with the exposure duration on the right panel. These data have been binned by four pixels to improve the S/N. No evidence for time-variation in the high-ion profiles is seen.

shallower for O VI than for C IV and Si IV in the range -90 to -50 km s^{-1} (see Sect. 4.3).

Three strong components of HV high-ion absorption are seen (Fig. 5), at velocities of -560 , -510 , and -370 km s^{-1} . The -560 and -510 km s^{-1} components are seen in C IV $\lambda 1548.204$, O VI $\lambda 1031.926$, O VI $\lambda 1037.617$, and C III $\lambda 977.020$, but are blended in C IV $\lambda 1550.781$ and absent in Si IV. The -370 km s^{-1} component is detected in C III, C IV, and Si IV, but the O VI profiles are fully saturated at this velocity. The NV data show no significant detection in the HV gas, though the S/N near the NV lines is too low to place a strong constraint on $N(\text{NV})$. Neutral-phase absorption is not seen in the three HV components, even in the sensitive (high f -value) lines O I $\lambda 1302.169$, Si II $\lambda 1260.422$, and C II $\lambda 1334.532$, with the single exception of a detection of weak C II at -370 km s^{-1} . The $N(\text{C IV})/N(\text{Si IV})$ ratios change dramatically between the various components, from 4.8 ± 1.0 at -110 km s^{-1} , to 40 ± 9 at -370 km s^{-1} , >140 (3σ) at -510 km s^{-1} and >110 (3σ) at -560 km s^{-1} .

3.6.1. Time-series observations of GRB 071031

The combined UVES spectrum of GRB 071031 (shown in Fig. 4) was formed by co-adding four useful individual exposures, with exposure times of 300, 600, 1200, and 2400 s (the sequence of increasing exposure times was chosen to compensate for the fading of the afterglow). Analysis of these individual frames allows us to look for time-variation in the high-ion absorption. We look for variation in the C IV and Si IV profiles, since these lines fall in parts of the spectrum where the S/N is highest (a NV time-series is unavailable). We focus on the HV components, since the high-ion absorption at z_{GRB} is saturated, making time-variation at that redshift difficult to detect. The time-series spectra are shown in Fig. 6. No evidence for any evolution in the C IV or Si IV profiles is seen. The lack of variation can be quantified by measuring the equivalent width at each observing epoch. The total equivalent width and 1σ error measurements in the range -600 to -330 km s^{-1} (over three HV components) are 266 ± 88 , 327 ± 49 , 233 ± 36 , and $306 \pm 30 \text{ m\AA}$ in the four exposures respectively, consistent with no variation in the absorption with time. Thus the behavior of the high-ion lines in these HV absorbers is in contrast to the time-variation in

low-ion and fine-structure absorption lines at z_{GRB} reported by Dessauges-Zavadsky et al. (2006) and Vreeswijk et al. (2007).

3.7. GRB 080310 $z_{\text{GRB}} = 2.4274$

Strong high-ion absorption is seen in O VI, N V, C IV, S IV, and Si IV centered within 50 km s^{-1} of z_{GRB} . The N V profile shows two components separated by $50 \pm 3 \text{ km s}^{-1}$ and with b -values of 18 ± 3 and $19 \pm 3 \text{ km s}^{-1}$. The S VI profiles are suggestive of absorption at z_{GRB} , but with very low S/N and an inconsistency between the absorption in $\lambda 933.378$ and in $\lambda 944.523$. For this reason, we do not attempt to derive a S VI column density. Similarly the S IV $\lambda 1062.662$ profile is too noisy to measure a reliable column, but we can measure a lower limit of $\log N(\text{S IV}) > 14.77$ over the velocity range -70 to 30 km s^{-1} . Combining this with the constraint $\log N(\text{S IV}^*) < 14.38$ (3σ) from the non-detection of S IV* $\lambda 1072.973$, we find $N(\text{S IV}^*)/N(\text{S IV}) < 0.41$. The C IV, Si IV, and O VI profiles show a clear negative-velocity absorption-line wing extending from -120 to -260 km s^{-1} . This is the most extended absorption-line wing in our sample. Finally, a HV absorber at -1400 km s^{-1} is seen (see Fig. 5) with two C IV components, one of which is very narrow ($b = 4 \pm 2 \text{ km s}^{-1}$). For this GRB-DLA we derive an HI column density $\log N(\text{HI}) = 18.80 \pm 0.10$ and a metallicity $[\text{O}/\text{H}]$ of -1.39 ± 0.10 . No ionization correction was applied since a charge-exchange reaction closely links O I and H I, implying $[\text{O I}/\text{H I}] \approx [\text{O}/\text{H}]$ (Field & Steigman 1971).

4. Discussion

The six high-ion absorption lines reported in this paper at velocities near z_{GRB} are Si IV, S IV, C IV, S VI, N V, and O VI, which trace the Si^{+3} , S^{+3} , C^{+3} , S^{+5} , N^{+4} , and O^{+5} ions, requiring energies of 33.5, 34.8, 47.9, 72.6, 77.5, and 113.9 eV for their creation, respectively (Morton 2003). A galactic ionizing spectrum, dominated by the integrated radiation from O and B stars, drops strongly above 54 eV, the He II ionization edge (Bregman & Harrington 1986). So whereas the ions Si^{+3} , S^{+3} , and C^{+3} can be photoionized in the ISM by starlight, the ions S^{+5} , N^{+4} , and O^{+5} cannot. We expect this to remain true in GRB host galaxies, even though they have been shown to harbor significant numbers of Wolf-Rayet stars (Hammer et al. 2006), since Wolf-Rayet spectra also show a strong break at 54 eV (Crowther 2007). Instead, the detection of the three ions S^{+5} , N^{+4} , and O^{+5} implies the presence of either a hard, non-stellar radiation source or hot, collisionally ionized gas.

In the seven GRB afterglow spectra in our sample, the median and standard deviation of $\log N(\text{O VI})$ at z_{GRB} is 15.12 ± 0.54 . For comparison, the median $\log N(\text{O VI})$ measured in 100 sight lines passing through the Milky Way halo is 14.38 (Wakker et al. 2003; Savage et al. 2003), rising to 14.80 when including the contribution from high-velocity clouds (Sembach et al. 2003). Turning to N V, we report a median $\log N(\text{N V}) = 14.03 \pm 0.49$ in the seven GRB spectra, whereas the median $\log N(\text{N V})$ in 32 Galactic halo sight lines is 13.45 (Indebetouw & Shull 2004). High-ion absorption in N V and O VI has also been observed in $z = 2-3$ DLA galaxies, with a median $\log N(\text{O VI}) = 14.77$ (Fox et al. 2007a), and 76 per cent of DLAs showing $\log N(\text{N V}) < 13.50$ (Fox et al. 2008, in preparation). Thus the column densities of O VI and N V seen at z_{GRB} are, in the mean, higher than those seen in the halo of the Milky Way and those in DLAs. The highly ionized Galactic ISM is a complex environment, with many physical processes

Table 9. High-ion column density ratios.

GRB ^a	$\frac{N(\text{C IV})}{N(\text{O VI})}$	$\frac{N(\text{C IV})}{N(\text{Si IV})}$	$\frac{N(\text{N V})}{N(\text{O VI})}$
At $z(\text{GRB})$			
050922C	*	*	0.21 ± 0.04
060607	*	7.6 ± 1.2	*
Blueshifted Wings			
050730	0.40 ± 0.25	3.7 ± 0.9	< 0.09
060607	*	> 13	*
071031	1.6 ± 0.4	3.2 ± 0.9	< 0.11
080310	0.55 ± 0.11	25 ± 4	< 0.05
HV components			
021004 -2900 km s^{-1}	*	5.1 ± 3.1	*
050730 -1550 km s^{-1}	*	3.7 ± 0.4	*
050820 -3660 km s^{-1}	*	> 24	*
060607 -1850 km s^{-1}	*	3.2 ± 0.5	*
071031 -560 km s^{-1}	0.19 ± 0.06	> 110	< 0.06
071031 -510 km s^{-1}	0.35 ± 0.10	> 140	< 0.07
071031 -370 km s^{-1}	*	40 ± 9	*
080310 -1400 km s^{-1}	*	> 36	*
Galactic Halo ^b	0.60 ± 0.47	3.46 ± 1.09	0.12 ± 0.07
LMC ^c	$< 0.09-0.59$	$1.5-2.5$	< 0.33
DLAs, $z = 2-3^d$	2.1 ± 0.7	5.4 ± 2.2	...
IGM, $z = 2-4$	0.35^e	16 ± 4^f	$< 0.23^g$

^a We report the observed column density ratios in different velocity regions: in the strong components seen at z_{GRB} , in the blueshifted wings, and in the HV absorbers. All limits are 3σ . In cases marked *, saturation, blending, or low S/N prevents the ratio from being measured reliably.

^b Mean $\pm 1\sigma$ in 16 Milky Way halo sight lines (Zsargó et al. 2003).

^c Range observed in LMC gas (not including H II regions) in four sight lines (Lehner & Howk 2007).

^d Mean $\pm 1\sigma$ in 10 DLAs (Fox et al. 2007a).

^e Median value among four IGM absorbers measured by Simcoe et al. (2006).

^f Median $\pm 1\sigma$ in 188 IGM absorbers (Boksenberg et al. 2003).

^g Measured in composite QSO spectrum by Lu & Savage (1993).

contributing to the production of the high ions, including conductive interfaces, turbulent mixing layers, shocks, expanding supernova remnants, and galactic fountain flows (Savage et al. 2003; Zsargó et al. 2003; Indebetouw & Shull 2004; Bowen et al. 2008), and there is no reason why the ISM in the host galaxies of GRBs should be any less complex.

With this in mind, we now discuss the various categories of high-ion absorption seen near z_{GRB} . Throughout this section, we refer the reader to Table 9, which summarizes the high-ion to high-ion column density ratios measured in the GRB afterglow spectra, and compares them to the ratios measured in various other astrophysical environments.

4.1. Strong absorption at z_{GRB}

We always detect strong high-ion absorption exactly at z_{GRB} ⁶, in the form of saturated O VI, C IV, and Si IV components, and (where the data are unblended) also in S IV and S VI. N V is present in 6/7 cases, with the advantage of being less saturated than the other high-ion lines. Because of this, N V is the best line

⁶ In two cases the velocity centroid of the strongest high-ion absorption component differs from the nominal GRB redshift (measured from the low-ion lines) by more than 10 km s^{-1} : for GRB 050922C the offset is 65 km s^{-1} , and for GRB 071031 the offset is 25 km s^{-1} . However, since the GRB redshifts are not known to better than a precision of several tens of km s^{-1} , these offsets are not significant, and we treat the strong high-ion absorption as arising exactly at z_{GRB} .

to investigate the line width and optical depth in the strong absorption components. In the six cases where NV is detected, we fit eight NV components, with b -values of 7 ± 3 , 9 ± 3 , 11 ± 2 , 14 ± 8 , 16 ± 3 , 18 ± 3 , 19 ± 3 and 28 ± 3 km s⁻¹. The median of these eight values is 16 km s⁻¹. A NV component formed in gas at 200 000 K, the temperature at which the production of NV by collisions is maximized (Gnat & Sternberg 2007), has a b -value of 15.4 km s⁻¹. Therefore, we are unable to rule out collisional ionization for the gas traced by NV.

4.1.1. Photoionized circumburst gas?

Noticing that the NV absorption at z_{GRB} tends to be stronger and narrower (in total velocity width) than the NV absorption observed in the Milky Way ISM and in DLAs, Prochaska et al. (2008b) have recently argued that the NV absorption components at z_{GRB} do not trace ISM material in the halo of the host galaxy, but rather arise in circumburst gas in the immediate vicinity of the GRB. Our high-resolution UVES dataset, covering a wider range of ionization states than has been observed before, allows us to investigate this intriguing idea.

Our data are consistent with the circumburst hypothesis in the cases of GRBs 021004, 050922C, and 071031, where we see strong, single components of NV at z_{GRB} , each with $\log N(\text{NV}) > 14.0$, aligned with other high ions including O VI with $\log N(\text{O VI}) \gtrsim 14.5$. For these cases, our new measurements of the O VI, S IV, and S VI column densities at z_{GRB} (listed in Tables 2, 4, and 7) could be used to constrain photoionization models of the circumburst region. However, in the remaining four spectra in our sample (GRBs 050730, 050820, 060607, and 080310) the situation is more complex. In each of these four cases, $\log N(\text{NV}) < 14.1$, and in two cases $\log N(\text{NV}) < 13.2$, i.e. the observed NV is *not* in excess of what is expected from the host galaxy's ISM. In two of these cases (GRBs 050730 and 080310) the NV absorption profiles show two components separated by a few tens of km s⁻¹ – this is not the signature of a single burst. In another case (GRB 050820) there is an offset of 110 km s⁻¹ between a single NV component and the strongest absorption in the other high ions. And finally, in the case of GRB 060607, no NV is detected at all. In addition to these case-by-case details, we repeat that the b -values of the detected NV absorption components at z_{GRB} are *not* particularly narrow, so photoionization is not required by the line widths (though it is not ruled out either).

4.1.2. Total ionized column density

We can further investigate the nature of the strong components seen at z_{GRB} by calculating the total column density of ionized hydrogen $N(\text{hot H II})^7$ contained in these components. To do this we have to correct for ionization and metallicity, so the calculation is only possible for cases where the nitrogen abundance has been measured in the DLA at z_{GRB} . This is true for three GRBs in our sample: $[\text{N}/\text{H}] = -3.16 \pm 0.10$ for GRB 050730, > -1.35 for GRB 050820, and < -4.09 for GRB 050922C (Prochaska et al. 2007b). The relationship between the NV and hot H II column densities can be written in the following way:

$$N(\text{hot H II}) = \frac{N(\text{NV})}{(N \text{ v}/N)(\text{N}/\text{H})_n} \frac{(\text{N}/\text{H})_n}{(\text{N}/\text{H})_i}, \quad (1)$$

⁷ Here we use the word “hot” simply to label the NV-bearing gas; the upper limit on the temperature is 215 000 K for the median NV b -value of 16 km s⁻¹.

where $(\text{N}/\text{H})_i$ denotes the nitrogen abundance in the ionized gas and $(\text{N}/\text{H})_n$ denotes the nitrogen abundance in the neutral gas (which is measured). We take the solar nitrogen abundance of $(\text{N}/\text{H})_{\odot} = 10^{-4.22}$ from Grevesse et al. (2007), and then $(\text{N}/\text{H})_n = 10^{[\text{N}/\text{H}]}(\text{N}/\text{H})_{\odot}$. If the gas is collisionally ionized, as would be appropriate for NV in the host galaxy ISM, $N \text{ v}/N < 0.25$ at all temperatures (Gnat & Sternberg 2007)⁸. Therefore we adopt 0.25 as the maximum allowed ionization fraction, corresponding to a minimum ionization correction of a factor of 4. If the ionized gas has the same metallicity as the neutral gas, so that the term $(\text{N}/\text{H})_n/(\text{N}/\text{H})_i$ in Eq. (1) is equal to one, then $N(\text{hot H II})$ is:

$$\begin{aligned} > 21.8 \text{ for GRB 050730 (which has } \log N(\text{H I}) = 22.15), \\ > 19.3 \text{ for GRB 050820 (which has } \log N(\text{H I}) = 21.00), \text{ and} \\ > 22.7 \text{ for GRB 050922C (which has } \log N(\text{H I}) = 21.55), \end{aligned}$$

where the results are lower limits since (a) we have used the smallest allowed ionization correction, and (b) they only apply to the NV-bearing gas, and H II may exist at other temperatures as well. Comparing the values of $N(\text{hot H II})$ and $N(\text{H I})$, we find the hot-ionized-to-neutral ratio $N(\text{hot H II})/N(\text{H I})$ takes values of > 0.4 and > 0.02 for GRBs 050730 and 050820, and > 13 for GRB 050922C. Whereas the first two values are modest, the GRB 050922C value is extremely (and implausibly) high – it requires over ten times as much mass in hot ionized gas in a single component as there is in neutral gas in the entire host galaxy. However, if the nitrogen abundance in the ionized gas was higher than in the neutral gas, so that $(\text{N}/\text{H})_n/(\text{N}/\text{H})_i < 1$, then solutions with lower $N(\text{hot H II})$ would be possible. Thus our calculation of the total ionized column density at z_{GRB} suggests that the nitrogen abundance is higher in the highly ionized gas than in the neutral gas (particularly for GRB 050922C); however, this calculation is inconclusive in determining whether the gas is circumburst or interstellar.

4.1.3. Photo-excitation modeling of $N(\text{S IV})$ and $N(\text{S IV}^*)$

Another method for distinguishing between circumburst gas and more distant interstellar gas is to look for absorption from fine-structure levels. In circumburst gas, UV pumping by GRB photons will populate the excited electronic levels, which decay and cascade to populate the fine-structure levels of the ground state (Prochaska et al. 2006; Chen et al. 2007; Vreeswijk et al. 2007). Because of the rapid fading of the afterglow, the level populations evolve in a non-equilibrium, time-dependent manner. Our data allow us to investigate this process in the S IV ion, since in four GRB spectra the combination of a detection of S IV $\lambda 1062.662$ and a non-detection of S IV* $\lambda 1072.973$ allows us to place an upper limit on the S IV*/S IV ratio at z_{GRB} . The Einstein A-value of the forbidden transition between the ground state of S IV and its fine-structure level is 7.7×10^{-3} s⁻¹ (taken from NIST; Ralchenko et al. 2008)⁹. In other words, in the absence of stimulated photo- and collisional de-excitation, the fine-structure level probed by the S IV* 1072.973 transition will decay in $1/A = 130$ s. In fully ionized gas (as expected near GRBs) there is no Lyman- α opacity and so the S IV lines (which lie shortward of Lyman- α) will not be shielded from UV radiation. For GRBs 021004, 050730, and 080310 we measure 3σ limits to the $N(\text{S IV}^*)/N(\text{S IV})$ ratio of < 0.08 , < 0.12 , and < 0.41

⁸ This is true for either equilibrium or non-equilibrium models. However, in the Prochaska et al. (2008b) GRB photoionization models, a NV ionization fraction as high as 0.6 is predicted.

⁹ See <http://physics.nist.gov/PhysRefData/ASD/index.html>

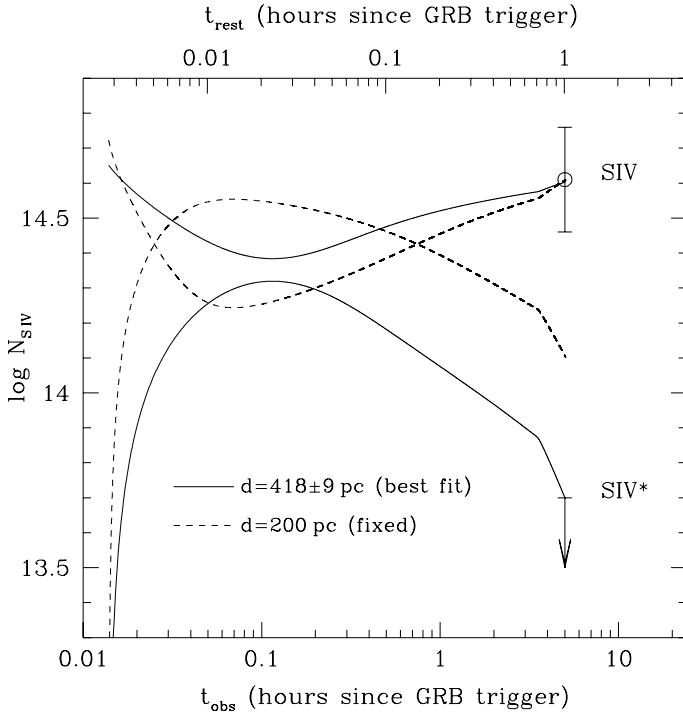


Fig. 7. Analysis of the S IV level populations at z_{GRB} toward GRB 050730. The solid and dashed lines show the predictions from UV photo-excitation models for the time-variation of the S IV and S IV* column densities (see text for details). The data points show the observed $N(\text{S IV})$ and upper limit to $N(\text{S IV}^*)$ in the UVES spectrum, plotted at the x -position corresponding to the mid-observation epoch (five hours after the trigger). The solid lines show the model with the best-fit distance of 418 ± 9 pc. The dashed lines show a model with the distance d fixed at 200 pc, for illustration. In this case $N(\text{S IV}^*)$ would be 0.5 dex stronger than observed, so this model is clearly ruled out. The result that the S IV-absorbing gas must lie at $d > 400$ pc implies an interstellar rather than circumburst origin.

respectively (for the other four afterglows we are unable to constrain this ratio due to blending).

Following the technique described in Vreeswijk et al. (2007), we can model the S IV excitation level in gas subject to UV radiation from the GRB, assuming that photo-excitation is the dominant excitation process. We chose to model the S IV level population measured toward GRB 050730, because this case has the strongest constraint on $N(\text{S IV}^*)$. The model has five free parameters: the distance d between the GRB and the absorbing gas (assuming all the S IV arises at the same distance), the total S IV column density N_{tot} (equivalent to the pre-burst ground-state S IV column density), the afterglow spectral slope β (where $F_{\nu} \propto \nu^{\beta}$), the Doppler b -parameter of the absorbing gas, and the rest-frame time when the calculation begins t_0 (i.e. the time when the afterglow photons begin to be tracked in the code). For a given set of these parameters, the model predicts the S IV and S IV* column densities as a function of time (both in the observer frame and in the rest frame). Since the time of mid-observation of GRB 050730 is known, five hours (observer frame) after the trigger, predicted values for $N(\text{S IV})$ and $N(\text{S IV}^*)$ can be extracted from each model.

The parameters in our GRB 050730 model were determined as follows. N_{tot} was chosen to equal $N(\text{S IV}) + N(\text{S IV}^*)$, assuming the actual $N(\text{S IV}^*)$ is equal to the measured upper limit (if the actual value is lower, our conclusions are strengthened; see below). The value for β (-0.56) was determined using the

observed light curve for this afterglow. The parameter t_0 is poorly constrained, but our runs showed that the S IV level populations are very insensitive to t_0 for values between 0 and 300 s; we used a value $t_0 = 10$ s (see Vreeswijk et al. 2007). Finally a b -value of 10 km s^{-1} was chosen as a typical value for interstellar gas, and indeed matches (within the $1\text{-}\sigma$ error) the measured b -value for the S IV component at 0 km s^{-1} toward GRB 050730. This leaves the distance d as the one genuinely floating parameter in the model; a grid of models at different distance d was generated, and the predicted and observed $N(\text{S IV})$ and $N(\text{S IV}^*)$ were compared using a chi-squared minimization routine.

The model results are shown in Fig. 7. The best-fit distance d is 418 ± 9 pc. Because we assumed that the actual S IV* column density was equal to the measured upper limit, this represents a strong lower limit of 400 pc (2σ) on the distance of the absorbing gas from the GRB. In other words, if the gas was at $d < 400$ pc, we would have seen S IV* absorption, whereas we clearly do not. This represents an important result, since it implies that the S IV absorption has an interstellar rather than circumburst origin. The distance limit on the S IV absorption does not necessarily have to apply to the N V absorption (or the other high ions). However, the N V and S IV profiles at z_{GRB} toward GRB 050730 are similar, both showing the component near 0 km s^{-1} and a weaker component at 25 km s^{-1} , suggesting that the two ions are co-spatial and hence that the N V absorption also arises at >400 pc from the GRB.

4.1.4. Origin of strong absorption

In summary, we find that while the circumburst hypothesis explains the observation that in three afterglow spectra, strong single-component N V is aligned with saturated absorption in the other high ions, it is challenged by the N V profiles in the other four datasets, it is not strictly required by the N V line widths, and the expected high-ion fine-structure lines and time-variable column densities are yet to be observed. Furthermore, in one case (GRB 050730) we are able to place a lower limit on the distance to the high-ion absorbing gas of 400 pc, using the simultaneous detection of S IV and non-detection of S IV*. Therefore, based on our current dataset, we cannot rule out an interstellar explanation for the strong high-ion components at z_{GRB} , noting that since the higher $N(\text{H I})$ values in GRB-DLAs than in QSO-DLAs suggest that GRB sightlines pass through the inner star-forming regions of the host galaxies (Prochaska et al. 2008a; Fynbo et al. 2008), one would expect high column densities of interstellar plasma at z_{GRB} , so the strength of the N V absorption does not, in our view, argue against an interstellar origin. We also note that a strong, apparently narrow (though unresolved) N V component is observed in the spectrum of LBG cB58 at the galaxy redshift ($z = 2.73$, Pettini et al. 2002), showing that such components can be formed even in the absence of a GRB. Time-series observations of N V in GRB afterglow spectra, which unfortunately are not available in the current dataset, would help to resolve this issue. A significant detection of time-variation in the N V column density at z_{GRB} (see models by Prochaska et al. 2008b) would represent the discovery of gas that is unambiguously close to the GRB.

4.2. Multi-component absorption in C IV and Si IV

The multi-component structure seen in C IV and Si IV spreading over several hundred km s^{-1} around z_{GRB} is not seen in the other high ions. However, the C IV and Si IV profiles lie out of the

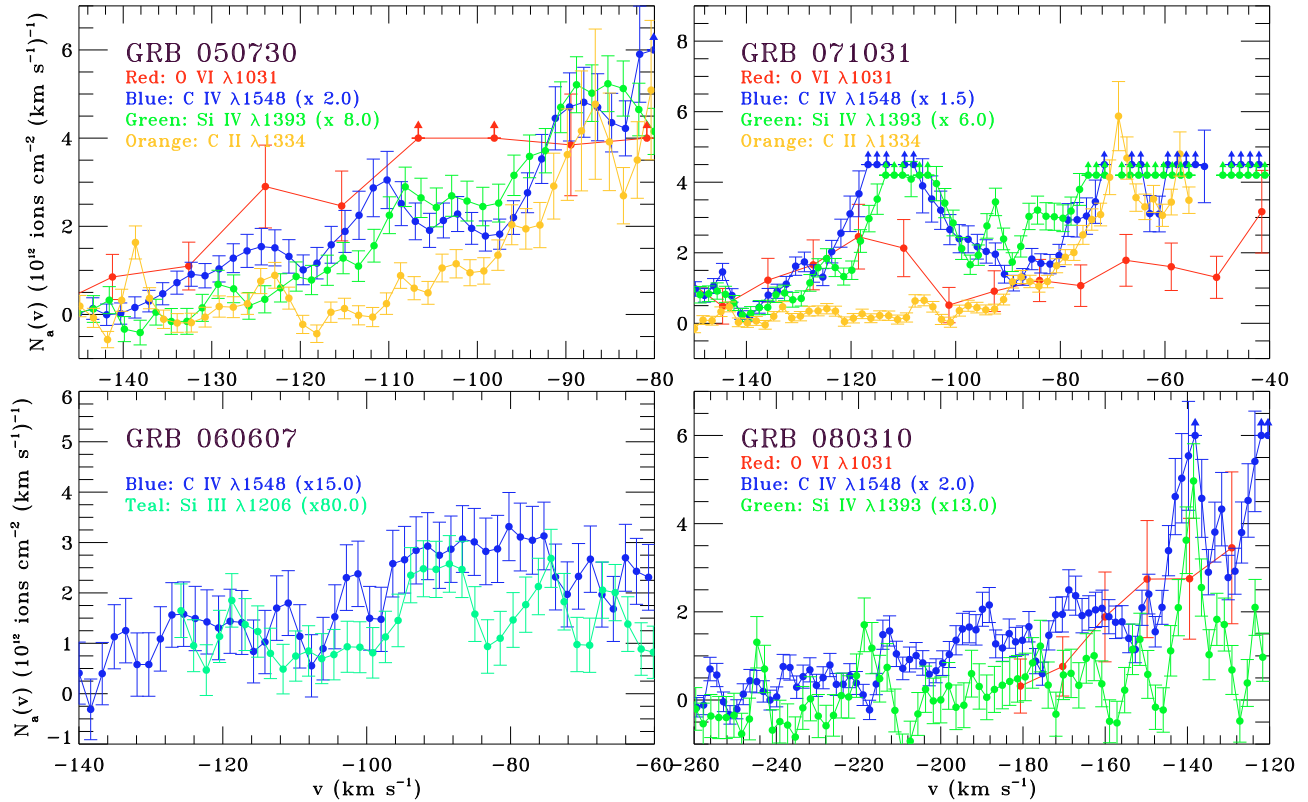


Fig. 8. High-ion apparent column density profiles in the four negative-velocity wings in our sample. Errors reflect both statistical noise and continuum placement uncertainties. The C IV and Si IV profiles have each been scaled by the factors annotated on the plot to allow for comparison of their shape with O VI. Only lower limits (arrows) can be presented for saturated pixels. The O VI data have been rebinned by four pixels in the case of GRB 071031, eight pixels in the case of GRB 050922C, and five pixels in the other cases. N V, S IV, and S VI are not detected in the wings.

Lyman- α forest, so are free from blending and show higher S/N than O VI or N V, and it is unclear how the O VI and N V profiles would appear if observed at the same S/N. These complex, multi-component Si IV and C IV profiles are reminiscent of the profiles of these ions in damped Lyman- α (DLA) absorbers (Lu et al. 1996; Ledoux et al. 1998; Wolfe & Prochaska 2000; Fox et al. 2007b; Lehner et al. 2008), which represent galaxy halos seen in absorption toward a background source. The median (mean) value of the total C IV velocity width in 74 DLAs and sub-DLAs at $z = 2-3$ reported by Fox et al. (2007b) is 255 km s^{-1} (342 km s^{-1}), where the width is the total observed range of absorption, regardless of optical depth. In the seven GRB spectra in our current sample, the median (mean) total C IV velocity width measured in an identical manner is 280 km s^{-1} (320 km s^{-1}), similar to the DLA value (note we have excluded the HV components, which we treat separately). A precise comparison of the median C IV column density between the GRB sample and the DLA sample is not possible, because these measurements are affected by saturation, but we can state that $\log N(\text{C IV})$ at z_{GRB} is ≥ 15 in all seven GRB spectra, which is significantly stronger than the median DLA value $\log N(\text{DLA C IV}) = 14.27 \pm 0.57$ measured by Fox et al. (2007b). Nonetheless, the similarities in total C IV line width between GRB and DLAs support a galactic origin for the multiple components seen in C IV and Si IV in a velocity range of several hundred km s^{-1} around z_{GRB} .

4.3. Negative-velocity (blueshifted) absorption-line wings

One notable feature present in four of the seven GRB afterglow spectra in our sample is a negative-velocity absorption-line

wing seen in C IV, Si IV, and (at lower S/N) O VI. These wings are characterized by relatively smooth, asymmetric absorption extending for $65-140 \text{ km s}^{-1}$ to negative velocities relative to the strong absorption at z_{GRB} . To explore the high-ion velocity structure in the wings, we present in Fig. 8 apparent column density profiles of the high ions over the velocity of the wings, calculated using $N_a(v) = 3.768 \times 10^{14} \tau_a(v) / f \lambda$, where the apparent optical depth $\tau_a(v) = \ln [F_c(v) / F(v)]$, $F(v)$ and $F_c(v)$ are the observed flux level and estimated continuum level as a function of velocity, and where λ is in \AA (Savage & Sembach 1991). We follow the error treatment of Sembach & Savage (1992). This form of display allows the velocity structure seen in each ion to be closely compared. In two cases we add the profile of C II $\lambda 1334.532$, which also shows wing absorption. The high-ion column densities in the wings are summarized in Table 10.

We find that the C IV and Si IV profiles track one another closely in three of the four wings, indicating that the two ions form in the same regions of gas. The exception is the very weak wing seen toward GRB 060607, in which Si IV is not detected, but Si III is seen. For the wings seen toward GRBs 050730 and 080310, the O VI and C IV profiles share a common gradient dN_a/dv . However, for GRB 071031, the O VI absorption shows a shallower slope. We measure a $N(\text{C IV})/N(\text{Si IV})$ ratio of ≈ 3 in two of the four wings (GRBs 050730 and 071031), similar to the Galactic halo average of 3.46 ± 1.09 measured by Zsargó et al. (2003). This supports an interstellar origin for the absorption-line wings. In the wings toward GRBs 060607 and 080310 the $N(\text{C IV})/N(\text{Si IV})$ ratio is much higher, taking values of > 13 (3σ) and 25 ± 4 respectively.

O VI absorption-line wings with similar velocity extent have been observed at zero redshift in the ultraviolet spectra

Table 10. Properties of absorption in the blueshifted wings.

GRB	z_{GRB}	$v_{\text{min}}, v_{\text{max}}^a$ (km s^{-1})	δv^b (km s^{-1})	$\log N(\text{O VI})$ (N in cm^{-2})	$\log N(\text{C IV})$ (N in cm^{-2})	$\log N(\text{Si IV})$ (N in cm^{-2})	$\log N(\text{N V})$ (N in cm^{-2})
050730	3.9686	-145, -80	65	14.47 ± 0.35	13.79 ± 0.03	13.21 ± 0.02	<13.56
060607	3.0749	-140, -60	80	...	13.00 ± 0.02	<12.27	<12.91
071031	2.6922	-150, -40	110	14.25 ± 0.06	14.45 ± 0.09	13.95 ± 0.06	<13.59
080310	2.4274	-260, -120	140	14.31 ± 0.08	14.05 ± 0.02	12.65 ± 0.06	<13.27

^a On velocity scale relative to z_{GRB} . ^b Velocity extent of wing $\delta v \equiv v_{\text{max}} - v_{\text{min}}$, shaded light grey in Figs. 2–4.

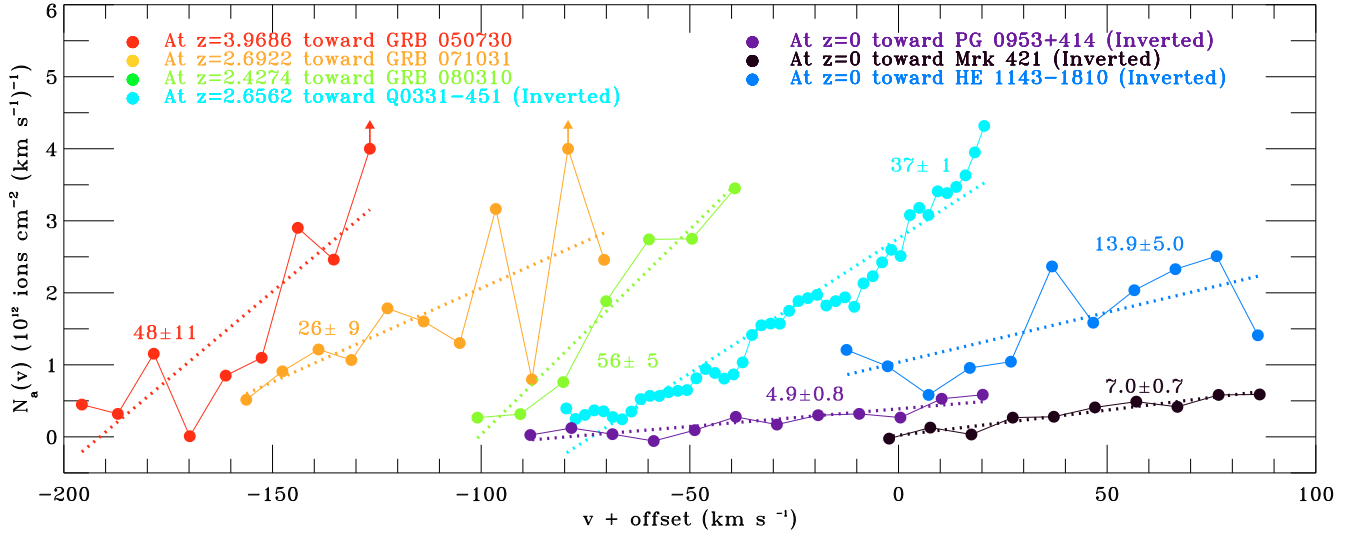


Fig. 9. Montage of apparent column density profiles of O VI absorption-line wings measured in various environments: near z_{GRB} in three GRB afterglow spectra (this paper, three left-most lines), at zero redshift in the Milky Way halo in the UV spectra of three AGN (Fox et al. 2006, three right-most lines), and in a sub-DLA at $z = 2.6562$ (Fox et al. 2007c). The Milky Way and sub-DLA cases have been inverted and velocity offsets have been added for ease of comparison, but the gradient of each profile is preserved. Linear fits are shown with color-coded dashed lines, and the gradient of each fit in units of 10^9 ions cm^{-2} (km s^{-1})⁻² is annotated with its 1σ error on the panel. In these diverse galactic environments sampling over twelve billion years, the O VI absorption-line profiles can be used to trace and quantify galactic outflows.

of quasars taken with the *Far-Ultraviolet Spectroscopic Explorer* (*FUSE*) satellite (Sembach et al. 2001, 2003; Fox et al. 2005, 2006; Savage et al. 2005a; Keeney et al. 2006)¹⁰. Fox et al. (2006) measured eleven Galactic O VI wings, and report a mean and standard deviation O VI column density of $\log N(\text{O VI}) = 13.85 \pm 0.45$, with each wing extending over ~ 100 km s^{-1} ; these authors successfully modeled the O VI absorption-line wings as tracing Galactic outflows moving under ballistic trajectories. Furthermore, a strong O VI wing covering a similar velocity range is seen in a sub-DLA (an absorber with $19.0 < \log N(\text{H I}) < 20.3$) at $z = 2.67$ (Fox et al. 2007c). The C IV profile observed in the LBG cB58 at $z = 2.7$ shows a clear absorption wing extending from -250 to -750 km s^{-1} (\approx nine resolution elements) in the galaxy rest-frame (Pettini et al. 2002), and an asymmetric blueshifted absorption feature in Mg II has been reported in the composite spectrum of 1400 $z \approx 1.4$ galaxies by Weiner et al. (2008), who also interpret it as a galactic outflow signature.

Whereas the $z = 0$ O VI wings are always detected at positive velocities (redshifted) relative to the Local Standard

of Rest (LSR), the GRB wings are seen at negative velocities (blueshifted) relative to z_{GRB} . This behavior is strongly suggestive of galactic outflows: in the Milky Way case (at least for high-latitude and anti-center sight lines, where Galactic rotation effects are insignificant), outflowing gas appears redshifted relative to the LSR, whereas in the GRB case, outflowing gas moves toward us along the line-of-sight and hence appears blueshifted relative to the host galaxy. The possibility remains that some wing absorbers represent chance alignments of unrelated components separated by small velocities, which are unresolved by the spectrograph. However, we find this explanation unlikely for the strongest wings in our sample, seen toward GRBs 071031 and 080310, since in these cases the column density in the wing increases monotonically with velocity¹¹ in an interval of over 100 km s^{-1} , and there is no reason why a series of random components should be aligned in this way.

To illustrate the similarity in the wing absorption features observed at both low and high redshift, we show in Fig. 9 a comparison of the O VI apparent column density profiles in the zero redshift and GRB sight line wings. We have inverted the positive-velocity wings to compare their gradient with the wings observed in the GRB spectra. While the similarity in the overall shapes of the wing profiles is striking, the high- z wings in the

¹⁰ Analogous C IV and Si IV wings are yet to be observed at zero redshift, but these two ions fall in the near-UV, requiring *HST* observations rather than *FUSE*, and the number of high-resolution QSO spectra taken with *HST* is small compared to the number of extragalactic sight-lines observed with *FUSE*.

¹¹ In the case of GRB 071031, the C IV profile shows a smooth gradient with velocity once the -115 km s^{-1} component has been subtracted off.

GRB host galaxies show higher O VI column densities (by a factor of ≈ 5) and steeper gradients dN_a/dv (by a factor of 5–10) than the Milky Way wings, implying higher mass flow rates.

4.4. High-velocity components at 500–5000 km s⁻¹

In six of our seven GRB spectra (all GRBs except 050922C), high-ion components at 500–5000 km s⁻¹ relative to z_{GRB} are observed (see Fig. 5). Such HV components have been observed before in GRB 020813 (Barth et al. 2003), GRB 021004 (Møller et al. 2002; Mirabal et al. 2003; Schaefer et al. 2003; Fiore et al. 2005; Lazzati et al. 2006), GRB 030226 (Klose et al. 2004), GRB 050505 (Berger et al. 2006), and GRB 050730 (D’Elia et al. 2007; Chen et al. 2007). Chen et al. (2007) report that C IV components with $W_r > 200$ mÅ occur at 1000–5000 km s⁻¹ in 20 per cent of GRB afterglow spectra. In our data, the incidence of HV C IV absorbers (6/7, or 86%) is much higher because (a) we have a higher sensitivity: the weakest HV C IV absorber in our sample shows $W_r = 48$ mÅ, and (b) we classify absorbers in the range 500–1000 km s⁻¹ as HV.

The HV absorbers seen in GRB afterglow spectra do not represent a homogeneous population, as do the blueshifted absorption-line wings and (potentially) the strong, narrow absorbers at z_{GRB} . On the contrary, we observe a broad range of properties among the HV absorbers. In three sight lines (toward GRBs 021004, 050730, and 060607), the HV components exhibit low-ionization absorption (clearest in C II $\lambda 1334.532$ and Si II $\lambda 1260.422$). However, the HV components toward GRBs 050820, 071031 and 080310 show no (or very weak) neutral-phase absorption, in either C II or Si II. So whereas the presence of neutral gas in the first three cases implies the absorbing material is not formed in the circumburst medium (because this medium is expected to be fully ionized by the burst; e.g. Vreeswijk et al. 2007; Chen et al. 2007; Prochaska et al. 2008b), we find that the properties of the HV components in the latter three cases *are* consistent with an origin in the close circumburst medium. This is particularly true for the HV gas toward GRB 071031, which is detected in the form of strong, O VI and C IV components that are not only absent in C II and Si II, but also show non-detections of Si IV. We have placed limits of $N(\text{CIV})/N(\text{SiIV}) > 110$ at -560 km s⁻¹, and > 140 at -510 km s⁻¹ in the GRB 071031 spectrum. These extreme ratios are far higher than typical interstellar values (Galactic ISM values for this ratio are ≈ 3 ; Zsargó et al. 2003) implying these HV components have a different, non-interstellar origin.

Given the connection between GRBs and massive stars (MacFadyen & Woosley 1999; Woosley & Bloom 2006), a leading explanation for the HV components in GRB afterglow spectra is that they trace outburst episodes from the massive-star progenitors of the GRBs (e.g. Schaefer et al. 2003), and thus arise in the circumburst region. As pointed out by Berger et al. (2006), a Wolf-Rayet outflow model would give rise to absorbers that are enriched in carbon and deficient in silicon, naturally explaining the high C IV/Si IV ratios measured in the HV absorbers.

If the wind-blown bubbles around GRB progenitors are similar in size to those observed around Wolf-Rayet stars in the Milky Way, their typical radius will be ≈ 2 –10 pc (Gruendl et al. 2000). Several groups have recently modeled Wolf-Rayet winds and their relationship to the HV components in GRB afterglow spectra (Ramirez-Ruiz et al. 2001, 2005; Chevalier et al. 2004; Eldridge et al. 2006), and in particular, predictions for the high-ion signature of Wolf-Rayet winds are given by van Marle et al. (2005, 2007, 2008). Depending on observing

epoch and viewing angle, components at 150–700 km s⁻¹ and 1000–2000 km s⁻¹ are predicted at various stages of Wolf-Rayet evolution (van Marle et al. 2005); these velocities match the observed range of HV components in our sample. Recent models of the absorption-line signatures of galactic winds (as opposed to single-star winds; Fangano et al. 2007; Kawata & Rauch 2007; Samui et al. 2008) generally predict high-ion components at velocities of only 100–200 km s⁻¹ relative to the galaxy, though observations support the idea that galactic winds can reach speeds of ≈ 1000 km s⁻¹ (Frye et al. 2002; Tremonti et al. 2007; Weiner et al. 2008). Nonetheless, the fairly narrow b -values measured in the HV components toward GRBs 071031 and 080310 (not to mention the lack of Si IV) are at odds with the broader, collisionally ionized components expected in galactic winds (Oppenheimer & Davé 2006). Thus we conclude that among the available models, Wolf-Rayet winds are the best explanation for the highly ionized HV components toward GRBs 071031 and 080310.

5. Summary

We have performed a systematic study of the high-ion absorption near z_{GRB} in seven GRB afterglow spectra observed with UVES. Three of the seven were observed within 15 minutes of the trigger by the *Swift* satellite. This search has provided high-resolution (6.0 km s⁻¹ FWHM) profiles of absorption in the ions O VI, N V, C IV, Si IV, S IV, and S VI. The spectra contain a wealth of useful information on the properties of circumburst and interstellar gas in the GRB host galaxies. We have presented the results of Voigt profile fits to the high-ion absorption. Analysis of the line profiles shows that several types of high-ion absorption exist at $z \approx z_{\text{GRB}}$, which we summarize in the following points.

1. We detect strong high-ion absorption components exactly at z_{GRB} , always in O VI, C IV, and Si IV, usually in N V, and occasionally (where the data are unblended) in S IV and S VI. The high-ion column densities are significantly higher than those seen in the Milky Way ISM and in DLAs. We focus on N V since it is the least saturated and hence best-measured high ion. In three of seven afterglow spectra, the strong N V absorption takes the form of a single component coincident in velocity with saturated absorption in the other high ions, appearing to support the recent conclusion of Prochaska et al. (2008b) that GRBs can photoionize N V in circumburst gas. However, in the remaining four cases, the N V absorption is either multi-component, offset from the other high-ions, or absent, and it is unclear whether the circumburst hypothesis can explain these cases. In addition, the N V b -values (median of 16 km s⁻¹) are not narrow enough to rule out collisional ionization. Finally, for GRB 050730 we have placed a lower limit on the distance to the S IV-absorbing gas of 400 pc, based on comparing photo-excitation models to the observed column density of S IV and upper limit to S IV*. This supports an interstellar (rather than circumburst) origin for the strong high-ion absorption components at z_{GRB} .
2. In addition to the strong component at z_{GRB} , the C IV and Si IV absorption exhibits complex, multi-component profiles extending over several hundred km s⁻¹ (excluding the HV components, which we treat separately). The median total C IV line width in our seven spectra is 280 km s⁻¹, similar to the value it takes in high-redshift DLA galaxies. This supports a galactic ISM origin for these multiple components.

3. We detect asymmetric, blueshifted absorption-line wings in the C IV, Si IV, and (at lower S/N) O VI profiles in four of the seven GRB afterglow spectra. These wings are similar in shape and velocity extent ($\approx 100\text{--}150\text{ km s}^{-1}$) to positive-velocity wings seen in O VI absorption at zero redshift in the Milky Way halo, and two of the four wings show C IV/Si IV ratios of ≈ 3 , equivalent to the value measured in the Milky Way ISM. We thus interpret the wings as tracing outflowing interstellar gas. The O VI column densities in the GRB wings are, in the mean, five times higher than the O VI column densities in the Milky Way wings (implying similarly higher mass flow rates), and the gradient dN_{a}/dv is typically 5–10 times higher.
4. HV ($500\text{--}5000\text{ km s}^{-1}$) components are seen in C IV in six of the seven spectra (all GRBs except 050922C). These components are not necessarily a single homogeneous population, and many may arise in unrelated foreground galaxies. However, in the (previously unpublished) cases of GRBs 071031 and 080310, the ionization properties of the HV components (very high C IV/Si IV ratios and an absence of neutral-phase absorption in Si II or C II) are consistent with a circumburst origin. Models of Wolf-Rayet winds from the GRB progenitor stars are capable of explaining the kinematics and ionization level of these HV components.

Acknowledgements. We thank the ESO staff for their implementation of the rapid-response mode. P.M.V. acknowledges the support of the EU under a Marie Curie Intra-European Fellowship, contract MEIF-CT-2006-041363. We thank Nicolas Lehner, Chris Howk, and Hsiao-Wen Chen for comments on the manuscript.

References

- Adelberger, K. L., Shapley, A. E., Steidel, C. C., et al. 2005, *ApJ*, 629, 636
- Arav, N., Korista, K. T., de Kool, M., Junkkarinen, V. T., & Begelman, M. C. 1999, *ApJ*, 516, 27
- Ballester, P., Modigliani, A., Boitquin, O., et al. 2000, *The Messenger*, 101, 31
- Barth, A. J., Sari, R., Cohen, M. H., et al. 2003, *ApJ*, 584, L47
- Berger, E., Penprase, B. E., Cenko, S. B., et al. 2006, *ApJ*, 642, 979
- Bloom, J. S., Kulkarni, S. R., & Djorgovski, S. G. 2002, *AJ*, 123, 1111
- Boksenberg, A., Sargent, W. L. W., & Rauch, M. 2003 [[arXiv:astro-ph/0307557](https://arxiv.org/abs/astro-ph/0307557)]
- Bowen, D. V., Jenkins, E. B., Tripp, T. M., et al. 2008, *ApJS*, 176, 59
- Bregman, J. N., & Harrington, J. P. 1986, *ApJ*, 309, 833
- Castro, S., Galama, T. J., Harrison, F. A., et al. 2003, *ApJ*, 586, 128
- Chen, H.-W., Prochaska, J. X., Bloom, J. S., & Thompson, I. B. 2005, *ApJ*, 634, L25
- Chen, H.-W., Prochaska, J. X., Ramirez-Ruiz, E., et al. 2007, *ApJ*, 663, 420
- Chevalier, R. A., Li, Z.-Y., & Fransson, C. 2004, *ApJ*, 606, 369
- Christensen, L., Hjorth, J., & Gorosabel, J. 2004, *A&A*, 425, 913
- Churchill, C. W., & Charlton, J. C. 1999, *AJ*, 118, 59
- Crowther, P. A. 2007, *ARA&A*, 45, 177
- Cummings, J. R., Baumgartner, W. H., Beardmore, A. P., et al. 2008, *GCN*, 7382
- Dekker, H., D'Odorico, S., Kaufer, A., Delabre, B., & Kotzłowski, H. 2000, *SPiE*, 4008, 534
- Dessauges-Zavadsky, M., Chen, H.-W., Prochaska, J. X., Bloom, J. S., & Barth, A. J. 2006, *ApJ*, 648, L89
- D'Elia, V., Melandri, A., Fiore, F., et al. 2005a, *GCN*, 3746
- D'Elia, V., Piranomonte, S., Fiore, F., et al. 2005b, *GCN*, 4044
- D'Elia, V., Fiore, F., Meurs, E. J. A., et al. 2007, *A&A*, 467, 629
- Eldridge, J. J., Genet, F., Daigne, F., & Mochkovitch, R. 2006, *MNRAS*, 367, 18
- Fangano, A. P. M., Ferrara, A., & Richter, P. 2007, *MNRAS*, 381, 469
- Field, G. B., & Steigman, G. 1971, *ApJ*, 166, 59
- Fiore, F., D'Elia, V., Lazzati, D., et al. 2005, *ApJ*, 624, 853
- Fox, A. J., Wakker, B. P., Savage, B. D., et al. 2005, *ApJ*, 630, 332
- Fox, A. J., Savage, B. D., & Wakker, B. P. 2006, *ApJS*, 165, 229
- Fox, A. J., Petitjean, P., Ledoux, C., & Srianand, R. 2007a, *A&A*, 465, 171
- Fox, A. J., Ledoux, C., Petitjean, P., & Srianand, R. 2007b, *A&A*, 473, 791
- Fox, A. J., Petitjean, P., Ledoux, C., & Srianand, R. 2007c, *ApJ*, 668, L15
- Frye, B. L., Broadhurst, T., & Benítez, N. 2002, *ApJ*, 568, 558
- Fynbo, J. P. U., Starling, R. L. C., Ledoux, C., et al. 2006, *A&A*, 451, L47
- Fynbo, J. P. U., Prochaska, J. X., Larsen, J. M., Dessauges-Zavadsky, M., & Møller, P. 2008, *ApJ*, 683, 321
- Ganguly, R., Sembach, K. R., Tripp, T. M., Savage, B. D., & Wakker, B. P. 2006, *ApJ*, 645, 868
- Gehrels, N., Chincarini, G., Giommi, P., et al. 2004, *ApJ*, 611, 1005
- Gnat, O., & Sternberg, A. 2007, *ApJS*, 168, 213
- Grevesse, N., Asplund, M., & Sauval, A. J. 2007, *Space Sci. Rev.*, 130, 105
- Gruendl, R. A., Chu, Y.-H., Dunne, B. C., & Points, S. D. 2000, *AJ*, 120, 2670
- Hammer, F., Flores, H., Schaerer, D., et al. 2006, *A&A*, 454, 103
- Hjorth, J., Møller, P., Gorosabel, J., et al. 2003, *ApJ*, 597, 699
- Holland, S. T., Barthelmy, S., Burrows, D. N., et al. 2005, *GCN*, 3704
- Indebetouw, R., & Shull, J. M. 2004, *ApJ*, 607, 309
- Jakobsson, P., Fynbo, J. P. U., Ledoux, C., et al. 2004, *A&A*, 427, 785
- Jakobsson, P., Fynbo, J. P. U., Ledoux, C., et al. 2006, *A&A*, 460, L13
- Jensen, B. L., Fynbo, J. P. U., Gorosabel, J., et al. 2001, *A&A*, 370, 909
- Kawata, D., & Rauch, M. 2007, *ApJ*, 663, 38
- Keeney, B. A., Danforth, C. W., Stocke, J. T., et al. 2006, *ApJ*, 646, 951
- Klose, S., Greiner, J., Rau, A., et al. 2004, *AJ*, 128, 1942
- Lazzati, D., Perna, R., Flasher, J., Dwarkadas, V. V., & Fiore, F. 2006, *MNRAS*, 372, 1791
- Ledoux, C., Petitjean, P., Bergeron, J., Wampler, E. J., & Srianand, R. 1998, *A&A*, 337, 51
- Ledoux, C., Vreeswijk, P. M., Ellison, S., et al. 2005, *GCN*, 3860
- Ledoux, C., Vreeswijk, P. M., Smette, A., Jaunsen, A., & Kaufer, A. 2006, *GCN*, 5237
- Ledoux, C., Jakobsson, P., Jaunsen, A. O., et al. 2007, *GCN*, 7023
- Lehner, N., & Howk, J. C. 2007, *MNRAS*, 377, 687
- Lehner, N., Fullerton, A. W., Massa, D., Sembach, K. R., & Zsargó, J. 2003, *ApJ*, 589, 526
- Lehner, N., Howk, J. C., Prochaska, J. X., & Wolfe, A. M. 2008, *MNRAS*, 390, 2
- Levshakov, S. A., Agafonova, I. I., Reimers, D., & Baade, R. 2003, *A&A*, 404, 449
- Lodders, K. 2003, *ApJ*, 591, 1220
- Lu, L., & Savage, B. D. 1993, *ApJ*, 403, 127
- Lu, L., Sargent, W. L. W., Barlow, T. A., Churchill, C. W., & Vogt, S. S. 1996, *ApJS*, 107, 475
- MacFadyen, A. I., & Woosley, S. E. 1999, *ApJ*, 524, 262
- Massa, D., Fullerton, A. W., Sonneborn, G., & Hutchings, J. B. 2003, *ApJ*, 586, 996
- Metzger, M. R., Djorgovski, S. G., Kulkarni, S. R., et al. 1997, *Nature*, 387, 878
- Mirabal, N., Halpern, J. P., Chornock, R., et al. 2003, *ApJ*, 595, 935
- Møller, P., Fynbo, J. P. U., Hjorth, J., et al. 2002, *A&A*, 396, L21
- Morton, D. C. 2003, *ApJS*, 149, 205
- Norris, J., Barbier, L., Burrows, D., et al. 2005, *GCN*, 4013
- Oppenheimer, B., & Davé, R. 2006, *MNRAS*, 373, 1265
- Page, M., Burrows, D., Beardmore, A., et al. 2005, *GCN*, 3830
- Penprase, B. E., Berger, E., Fox, D. B., et al. 2006, *ApJ*, 646, 358
- Pettini, M., Steidel, C. C., Adelberger, K. L., Dickinson, M., & Giavalisco, M. 2000, *ApJ*, 528, 96
- Pettini, M., Rix, S. A., Steidel, C. C., et al. 2002, *ApJ*, 569, 742
- Prochaska, J. X., Chen, H.-W., & Bloom, J. S. 2006, *ApJ*, 648, 95
- Prochaska, J. X., Chen, H.-W., Bloom, J. S., et al. 2007a, *ApJS*, 168, 231
- Prochaska, J. X., Chen, H.-W., Dessauges-Zavadsky, M., & Bloom, J. S. 2007b, *ApJ*, 666, 267
- Prochaska, J. X., Chen, H.-W., Wolfe, A. M., Dessauges-Zavadsky, M., & Bloom, J. S. 2008a, *ApJ*, 672, 59
- Prochaska, J. X., Dessauges-Zavadsky, M., Ramirez-Ruiz, E., & Chen, H.-W. 2008b, *ApJ*, 685, 344
- Ralchenko, Y., Kramida, A. E., Reader, J., and NIST ASD Team 2008, NIST Atomic Spectra Database, version 3.1.5, National Institute of Standards and Technology, Gaithersburg, MD
- Ramirez-Ruiz, E., Dray, L., Madau, P., & Tout, C. A. 2001, *MNRAS*, 327, 829
- Ramirez-Ruiz, E., García-Segura, G., Salmonson, J. D., & Pérez-Rendón, B. 2005, *ApJ*, 631, 435
- Ricker, G. R., Atteia, J.-L., Crew, G. B., et al. 2003, in *Gamma-Ray Burst and Afterglow Astronomy 2001*, ed. G. R. Ricker & R. K. Vanderspek (New York: AIP), AIP Conf. Proc., 662, 3
- Samui, S., Subramanian, K., & Srianand, R. 2008, *MNRAS*, 385, 783
- Savage, B. D., & Sembach, K. R. 1991, *ApJ*, 379, 245
- Savage, B. D., Sembach, K. R., Wakker, B. P., et al. 2003, *ApJS*, 146, 125
- Savage, B. D., Wakker, B. P., Fox, A. J., & Sembach, K. R. 2005a, *ApJ*, 619, 863
- Savage, B. D., Lehner, N., Wakker, B. P., Sembach, K. R., & Tripp, T. M. 2005b, *ApJ*, 626, 776
- Savaglio, S., & Fall, S. M. 2004, *ApJ*, 614, 293
- Savaglio, S., Fiore, F., Israel, G., et al. 2002, *GCN*, 1633

- Savaglio, S., Fall, S. M., & Fiore, F. 2003, *ApJ*, 585, 638
- Savaglio, S., Glazebrook, K., & Le Borgne, D. 2008, *ApJ*, submitted [arXiv:0803.2718]
- Schaefer, B. E., Gerardy, C. L., Höflich, P., et al. 2003, *ApJ*, 588, 387
- Sembach, K. R., & Savage, B. D. 1992, *ApJS*, 83, 147
- Sembach, K. R., Howk, J. C., Savage, B. D., Shull, J. M., & Oegerle, W. R. 2001, *ApJ*, 561, 573
- Sembach, K. R., Wakker, B. P., Savage, B. D., et al. 2003, *ApJS*, 146, 165
- Shirasaki, Y., Graziani, C., Matsuoka, M., et al. 2002, *GCN*, 1565
- Shapley, A. E., Steidel, C. C., Pettini, M., & Adelberger, K. L. 2003, *ApJ*, 588, 65
- Simcoe, R. A., Sargent, W. L. W., Rauch, M., & Becker, G. 2006, *ApJ*, 637, 648
- Starling, R. L. C., Vreeswijk, P. M., Ellison, S. L., et al. 2005, *A&A*, 442, L21
- Stroh, M. C., Gronwall, C., Grupe, D., et al. 2007, *GCN*, 7020
- Thöne, C. C., Greiner, J., Savaglio, S., & Jehin, E. 2007, *ApJ*, 671, 628
- Thöne, C. C., Fynbo, J. P. U., Östlin, G., et al. 2008a, *ApJ*, 676, 1151
- Thöne, C. C., Wiersema, K., Ledoux, C., et al. 2008b, *A&A*, 489, 37
- Tremonti, C. A., Moustakas, J., & Diamond-Stanic, A. M. 2007, *ApJ*, 663, L77
- van Marle, A. J., Langer, N., & García-Segura, G. 2005, *A&A*, 444, 837
- van Marle, A. J., Langer, N., & García-Segura, G. 2007, *A&A*, 469, 941
- van Marle, A. J., Langer, N., Yoon, S.-C., & García-Segura, G. 2008, *A&A*, 478, 769
- van Paradijs, J., Groot, P. J., Galama, T., et al. 1997, *Nature*, 386, 686
- Vilkoviskij, E. Y., Efimov, S. N., Karpova, O. G., & Pavlova, L. A. 1999, *MNRAS*, 309, 80
- Vreeswijk, P. M., Ellison, S. L., Ledoux, C., et al. 2004, *A&A*, 419, 927
- Vreeswijk, P. M., Ledoux, C., Smette, A., et al. 2007, *A&A*, 468, 83
- Vreeswijk, P. M., Jakobsson, P., Jaunsen, A. O., & Ledoux, C. 2008, *GCN*, 7391
- Wakker, B. P., Savage, B. D., Sembach, K. R., et al. 2003, *ApJS*, 146, 1
- Watson, D., Fynbo, J. P. U., Ledoux, C., et al. 2006, *ApJ*, 652, 1011
- Weiner, B. J., Coil, A. L., Prochaska, J. X., et al. 2008, *ApJ*, submitted [arXiv:0804.4686]
- Wiersema, K., Savaglio, S., Vreeswijk, P. M., et al. 2007, *A&A*, 464, 529
- Wolfe, A. M., & Prochaska, J. X. 2000, *ApJ*, 545, 591
- Wolfe, A. M., Gawiser, E., & Prochaska, J. X. 2005, *ARA&A*, 43, 861
- Woolsey, S. E., & Bloom, J. S. 2006, *ARA&A*, 44, 507
- Ziaeeepour, H. Z., Barthelmy, S. D., Gehrels, N., et al. 2006, *GCN*, 5233
- Zsargó, J., Sembach, K. R., Howk, J. C., & Savage, B. D. 2003, *ApJ*, 586, 1019